Research Square

Preprints are preliminary reports that have not undergone peer review.
They should not be considered conclusive, used to inform clinical practice,
or referenced by the media as validated information.

Thermal Conditioning of Moisture-Aged FFF Polymer Filaments for Recovering Print Quality, Morphology, and Mechanical Performance

Agus Widyianto
aguswidyianto@uny.ac.id
Universitas Negeri Yogyakarta
Yosef Budiman
Universitas Negeri Yogyakarta
Heri Wibowo
Universitas Negeri Yogyakarta
Moch Solikin
Universitas Negeri Yogyakarta
Dhany Arie Saputra
Universitas Negeri Yogyakarta
Nugraha Rizqi Saputra
Universitas Negeri Yogyakarta

Research Article

Keywords: Fused filament fabrication, Filament drying, Moisture absorption, Polymer filaments, Mechanical recovery, Thermal conditioning

Posted Date: June 12th, 2026

DOI: https://doi.org/10.21203/rs.3.rs-9806656/v1

License: This work is licensed under a Creative Commons Attribution 4.0 International License.
Read Full License

Additional Declarations: No competing interests reported.

Version of Record: A version of this preprint was published at Progress in Additive Manufacturing on October 22nd, 2026. See the published version at https://doi.org/10.1007/s40964-026-02026-7.

Thermal Conditioning of Moisture-Aged FFF Polymer Filaments for Recovering Print Quality, Morphology, and Mechanical Performance

Abstract

Hygroscopic filaments such as PLA+, PETG and ABS are sensitive to moisture of the polymer feedstock when extruded by fused filament fabrication (FFF). Outdoor storage causes moisture uptake, extrusion instability, layer defects and mechanical degradation of printed items. The drying-based recovery of moisture aged filaments is less well studied than filament storage or material modification. The material-specific heat conditioning was verified on the recovery of the PLA+, PETG, and ABS filaments stored outside. A temperature-time controlled filament dryer was designed and verified using embedded temperature monitoring, infrared thermography and transient thermal modeling. The recovery response was evaluated by SEM observation of the fracture surface, macroscopic surface comparison, gravimetric moisture, tensile and flexural load–displacement behaviors, and multivariate statistical analysis. Over time, the open storage led to increases in moisture and the degradation of mechanical performance. In contrast regulated drying improved print quality and load bearing capacity. The optimum drying temperature and time for PLA+ was 55 °C for 5 h, PETG was 65 °C for 5 h, and ABS was 75 °C for 5 h. Thermal validation showed constant and uniform heating of sensors, simulated temperature fields and infrared images. MANOVA results indicate significant effects of the drying stage and filament type on the mechanical responses (Wilks' Lambda: 0.292 and 0.345, $p < 0.001$). PCA also showed material grouping after drying, supporting a polymer specific recovery process. Thermal conditioning to improve reliability of moisture-aged FFF polymer filament is feasible and reproducible.

Keywords: Fused filament fabrication; Filament drying; Moisture absorption; Polymer filaments; Mechanical recovery; Thermal conditioning

1. Introduction

In recent years, innovations in additive manufacturing, particularly fused filament fabrication (FFF), have transformed perspectives on products, design, and prototyping. Through 3D printing, FFF offers an economical, feasible, and versatile solution for creating complex, customizable, high-precision objects from fromrmoplastic polymers [1] [2]. Basically, FFF works by building a physical object from a digital model through gradual

material deposition, layer by layer [3]. The multi-layered construction of 3D printed products from digital models enables greater design freedom and better material efficiency [4], resulting in less material waste compared to traditional formative and subtractive manufacturing [5], such as computer numerical control (CNC) [6]. Additionally, it offers low-cost fabrication with less energy [7], making it reliable for industrial applications. Due to the advantages outlined above, rapid development in additive manufacturing has occurred. It covers a wide range of applications, including aviation and space, automotive, electronics, biomedical, and so on[8]. During additive manufacturing, thermoplastic filaments are melted and extruded through a nozzle; the molten material is deposited onto a heated build plate, where it cools rapidly and solidifies. This process is repeated until the top layer is complete, and the product is finished.

It has been observed that common thermoplastic filaments are polylactic acid (PLA), polyethylene terephthalate glycol (PETG), and acrylonitrile butadiene styrene (ABS). PLA is a biodegradable material produced from natural resources that has the proper mechanical and chemical properties with minimal greenhouse gas (GHG) emissions [9]. In contrast to PLA derived from bio-sources, ABS is an engineering plastic that has butadiene groups evenly distributed in an acrylonitrile-styrene matrix [10], while PETG, derived from synthetic PET and glycol, exhibits strong chemical resistance and considerable impact strength [11]. Compared to ABS and PETG, PLA's tensile strength is higher, and it is easier to work with [12], making it stiffer than other pure filaments [13] and ideal for moldable applications. In addition, ABS material has higher stiffness than PETG [14]. Thus, these materials offer higher tensile strength and toughness; however, these properties are lower than those of PLA. It is suitable for applications that require a balance between impact and heat resistance. By contrast, PETG provides better elongation at break than PLA and ABS [15], making it suitable for applications that require strength, flexibility, and ease of printing.

These materials are considered hygroscopic, capable of absorbing moisture from the air [16] [17], making them sensitive to changes in humidity. Research by Huang et al. [18] highlighted that many users, particularly in educational settings and the handicraft industry, still rely on open storage, the simplest method for storing filaments. This reliance results in ongoing moisture issues that affect print consistency. When moisture diffuses into the filament’s amorphous zones, it behaves like a plasticizer, loosening molecular entanglements and weakening intermolecular bonds [19]. These phenomena cause polymer degradation [20], alter polymer chain bonds, and affect material performance, often resulting in poor printing quality [20]. Moreover, moisture in the filaments can induce swelling, as reported by Lendvai et al. [22], who observed a 5% increase in filament diameter, potentially leading to clogging.

Therefore, filament storage is essential to maintain quality and prevent moisture exposure. In addition to storage, filament is typically dried before melting in industrial settings to prevent degradation. In contrast, many 3D printer users skip this step. Hence, the quality of printed parts ultimately depends on ambient conditions that can vary with multiple factors, including geographic location. Furthermore, Andreozzi et al. [21] reported that filaments with lower moisture content generally produce printed parts with improved structural integrity, with a 15% increase in tensile strength and an 11.5% increase in flexural strength.

Moisture absorption can be due to the filament's porosity or its hygroscopic properties [22]. Therefore, various approaches are used to reduce the water content in filaments, including the development of storage techniques and material modification. According to the storage techniques, many researchers focus on developing beads or desiccant systems to absorb moisture content from 3D printing filaments. Lertsarawut et al. [23] developed a novel water-absorbing superpolymer (SAP) bead that could exhibit rapid water absorption, reaching equilibrium within hours, while an experimental evaluation on a green desiccant system using PW-PLA to overcome conventional air dehumidification systems was conducted by Comino et al. [24], resulting in the highest adsorption capacity of up to 12.7%. Meanwhile, Rafat et al. [25 reported a study of a coated desiccant that can absorb 1.12 g of water/g desiccant and increase the absorption cycle by up to 52%.

On the other hand, material development also accounts for a large share of research. Słowiński et al. [26] modified PETG with carbon fibers, thereby increasing the elastic modulus and improving resistance to moisture absorption. On the other hand, Vicente et al. [27] applied a protective coating by painting, resulting in a significant decrease in water absorption of up to 38%. Moreover, Filgueira et al. [28] examined the effect of enzymatic modification on filaments to improve interfacial adhesion and prevent water absorption.

Based on the literature review above, it can be concluded that most existing research focuses on the development of filament storage systems and material modification. However, our observations indicate that research on processing 3D-printing filaments to reduce water absorption through drying techniques remains limited. Moreover, in real-world settings, most current studies do not evaluate drying techniques for their direct impact on print quality indicators. This discrepancy highlights the need for empirical studies to identify ideal drying techniques. To overcome these limitations, this article presents a new approach to assessing the influence of drying techniques on filament properties, using a modified filament dryer to measure the moisture content removed. To identify novelty and research gaps, we examined previous studies, one of which was conducted by Limpadapun and Sukmanee [29] who

reported that this method can reduce the moisture concentration on PLA filament to 0.75 – 1.87% by weight for different times between 1 – 6 hours and temperatures of 40, 50, and 60 °C.

On the other hand, Hamid et al. [30] also performed a predrying treatment on PLA filaments. They reported that the undried specimens in SEM images exhibited more voids and evidence of incomplete diffusion, with moisture causing wider gaps between layers. By contrast, the predried specimens had fewer voids, improved diffusion, and better overall layer formation than the undried specimens. The literature suggests that the drying approach is a promising alternative to storage development and material modification.

Therefore, the drying process on various types of filaments for five hours at temperatures of 55, 65, and 75 °C, including PLA+, PETG, and ABS that have been left in open storage conditions for several weeks (4 weeks), is adapted as the main novelty, as well as building a modified filament dryer with an intelligent controller as an additional novelty. The device is equipped with a heating element and a humidity-control system to dry and store filaments simultaneously. Through a comprehensive evaluation, this study aims to: 1) measure the performance of the modified filament dryer, 2) determine the effect of open storage on the filament properties, 3) compare the properties of the filament before and after drying, and 4) provide an optimal drying strategy that can improve the reliability and quality of the filaments used thereafter. Furthermore, we deepened our analysis of the dried results of open-storage filaments by comparing the mechanical properties, surface appearance, and thermal contours through numerical simulations to determine the behavior of filaments during the drying process between newly used filaments and filaments that have been used for an extended period of time, thus making this research gap unique. In parallel, we expanded the manuscript with additional evidence, including SEM micrographs and time-series drying-temperature profiles for each specimen.

With a deep understanding of the critical parameters governing the filament recovery process, engineers and designers can make informed decisions regarding the reuse of their filament. The application of optimization techniques to reduce moisture content during the drying process enables industry adoption to restore filament performance and, in everyday use, results in fewer print-and-reprint failures, more consistent tensile and impact properties across the spool, and shorter printer setup times through repeatable pre-press conditioning steps. This approach can be readily implemented in manufacturing and service with several benefits, including reduced scrap and material costs, stabilization of component strength so that the final part behaves predictably, and support for circularity programs that reclaim partially used or

water-exposed spools. As a result, integrating drying with FFF ensures that reused filament produces reliable, high-quality parts suitable for a wide range of applications.

2. Materials and Methods

2.1. Research Procedure

To provide a clearer insight into this research, Figure 1 visualizes the research workflow. We developed a bench-scale filament-drying system through an iterative process that included 3D conceptual design, fabrication of a physical prototype, and electronic inspection for safety and functional integrity. Prototypes that failed inspection were revised until compliance was achieved. In parallel, polymer filaments were prepared and characterized in the form of specimens in accordance with accepted American Society for Testing and Materials ASTM standards and were suitable for establishing mechanical test results. To simulate degradation during use, the used filament rolls were stored in open air for 4 weeks and then re-characterized to assess the effects of water absorption on mechanical performance. Furthermore, the filament dryer was applied to the exposed filaments, after which the material was re-characterized with the same test matrix to ensure direct comparability: mechanical and thermal analyses, surface assessment, and statistical evaluation of replicate measurements. This design allows direct quantitative comparisons among fresh, moisture-exposed, and dried conditions, with sufficient replication for statistical analysis.

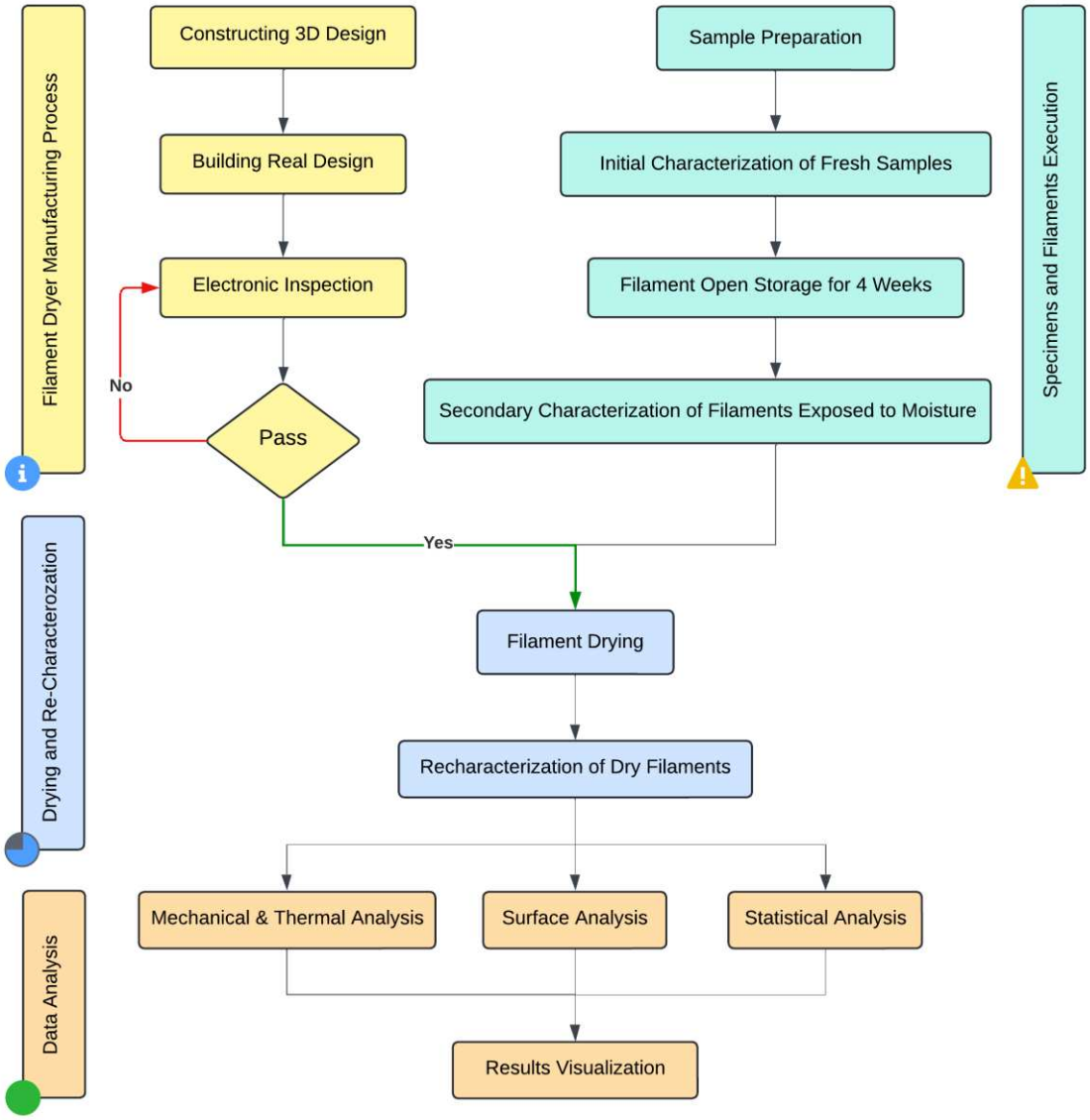


Figure 1. Research workflow

2.2. Design of Filament Dryer

The design of filament dryers is a crucial component of 3D printing filament preparation. This dryer is designed to reduce the filament's moisture content, ensuring optimal print quality and preventing issues such as bubbles, tangles, and warping. The following is a 3D model of the filament dryer and its components, created using Computer-Aided Design (CAD). The CAD process was performed in SolidWorks at a 1:1 scale. In general, the design of a filament dryer is similar to that of a typical oven, as shown in Figure 2 and Table 1. Filament dryer design focuses on creating an efficient system for removing moisture from 3D printing

filaments, which is essential for achieving optimal print quality. The process begins with defining the drying objectives for various filament types, such as PLA, PETG, and ABS.

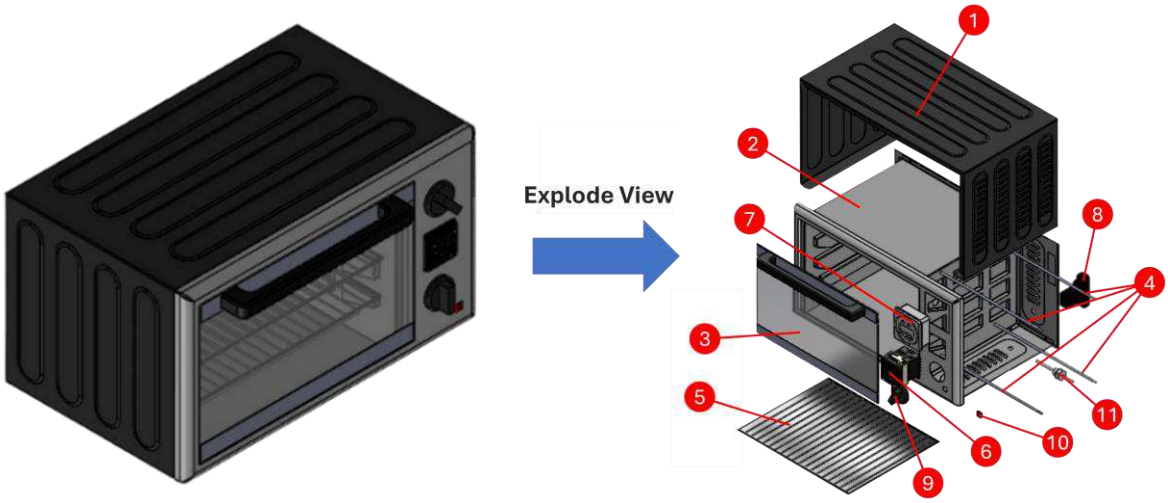


Figure 2. 3D design of filament dryer

Table 1. The bill is part of a filament dryer

Annotation Number	Part Name
1	Cover
2	Box
3	Glass Door
4	Heat Element
5	Shelf Support
6	Controller Omron E5CC
7	Programable Timer CN101A
8	Relay Omron MY2
9	Heat Mode Selector
10	Indicator Lamp
11	Omron MY2-P6DY PT100

Through comprehensive research and analysis, existing drying technologies were examined, along with the hygroscopic properties of the target material. However, the existing design required several modifications. The modification process involved replacing the heating system and adding control components to support the operation of the filament dryer. The modifications were intended to make the heating temperature and duration more flexible and applicable to a range of drying requirements across all filament types. Therefore, the filament dryer in this study offers multiple modes tailored to the appropriate filament type, automatically adjusting heating time and temperature without requiring extensive settings.

2.3. Procedure of Drying Process

The drying method used in this study was evaporation. This method was chosen because the filament is a solid substance that should not be contaminated with other substances. The filaments, exposed to air for 4 weeks, were dried in a filament dryer for 5 hours at 55°C, 65°C, and 75°C. After drying at specified temperatures and under temperature variations, the filaments were reprinted using a 3D printer to form a mechanical test specimen (see Figure 3). The drying process is important for determining the effect of each variation on the specimen's properties by comparing the specimen results before drying (with water content) and after drying (without water content).

2.4. Specimen Preparation

All specimens (18 specimens) in each week were fabricated by fused-filament fabrication (FFF) using a BIQU B1-series 3D printer to ensure repeatable, tool-controlled geometry and thermomechanical history across specimens. Selected filaments, including PLA+, PETG, and ABS with 1.75 mm diameter, were printed at a nominal height of 0.20 mm as shown in Table 2. Each test filament used is from a commercial product, namely eSUN or SUNLU. To create solid specimens, the temperature of each material was set at different points, 215 °C (PLA+), 250 °C (PETG), and 230 °C (ABS), paired with heated bed set points of 60 °C, 80 °C, and 100 °C, respectively, to enhance adhesion between layers while minimizing warpage.

Table 2. 3D printer parameters

Parameters	Material			Unit
	PLA +	PETG	ABS	
Nozzle Diameter	0.4	0.4	0.4	mm
Filament Diameter	1.75	1.75	1.75	mm
Layer Height	0.2	0.2	0.2	mm
Fill Pattern	Concentric	Concentric	Concentric	-
Infill Density	50	50	50	%
Print Speed	70	50	50	mm/s
Nozzle Temperature	215	250	230	°C
Bed Temperature	60	80	100	°C
Layer Thickness	0.2	0.2	0.2	mm
Wall Thickness	1.2	1.2	1.2	mm

Before printing each specimen, the printer was leveled, the extrusion flow was verified using a single-wall calibration, and the G-Code was kept constant regardless of the set temperature to isolate material effects from processing variability. Immediately before printing,

the first 100 mm of filament was purged to remove any material that had resided in the melt zone during heating. We also standardized key print parameters to improve comparability and quality, including a 0.4 mm nozzle, a 0.2 mm layer thickness, and print speeds of 70, 50, and 25 mm/s for PLA+, PETG, and ABS, respectively. As shown in Figure 3, specimens were fabricated on the concentric contour to stabilize the gauge section edges at 50% infill density. Rismalia et al. [31] studied the effect of the tensile properties of 3D-printing filaments on different infill patterns. They found that the concentric pattern exhibited the highest tensile properties, thereby being the optimal setting with respect to the printing parameters.

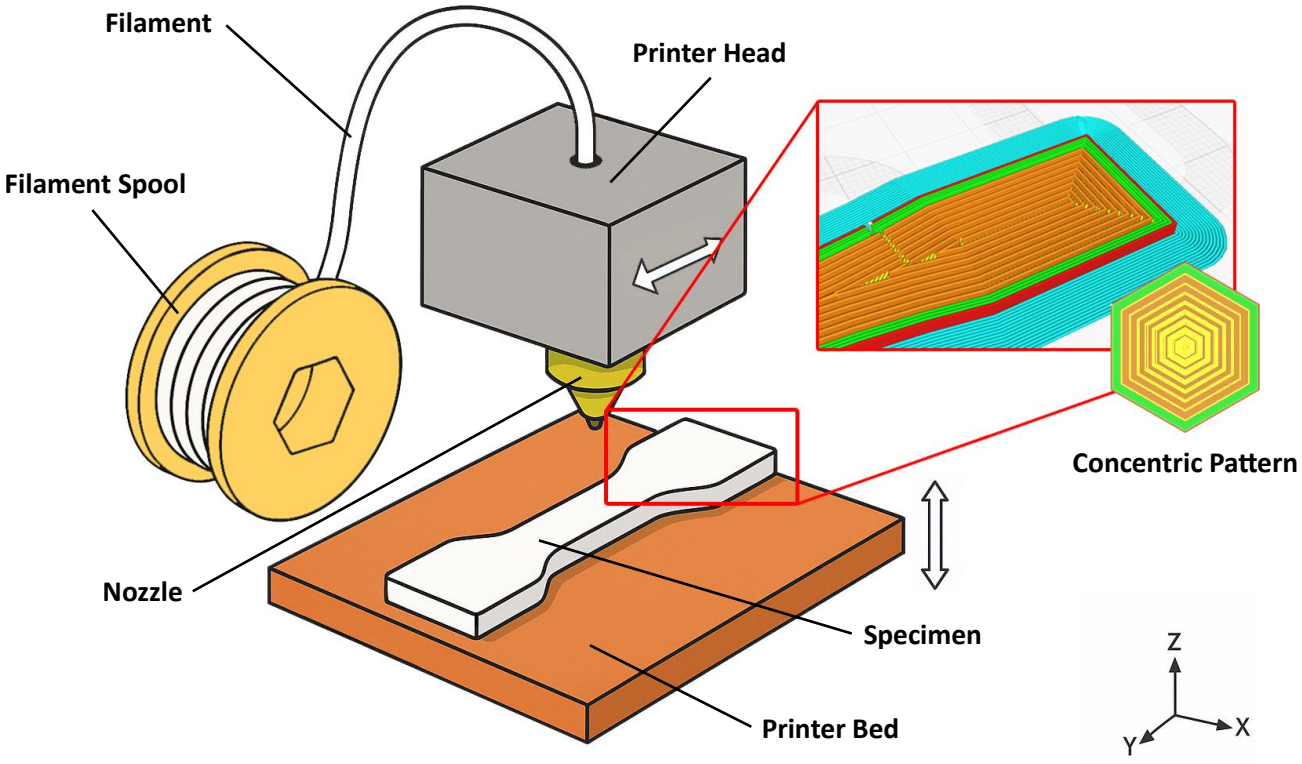


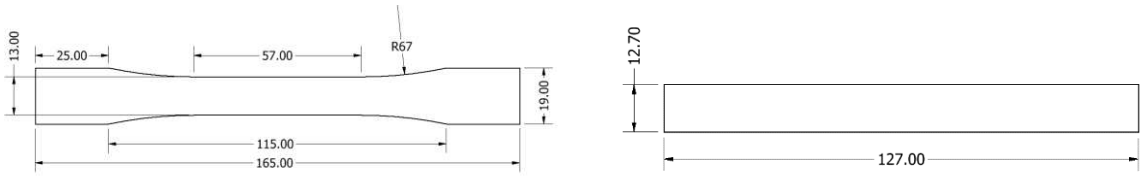
Figure 3. 3D printing schematic process

Furthermore, the component is printed in the XY plane with the long axis parallel to X. At this stage, the polymer filament is melted using a heated nozzle and carefully spread layer by layer to form the component. Afterward, the printed specimen is left on the bed for 30 minutes to reach room temperature and solidify, then stored in an airtight bag until testing.

2.5. Mechanical Testing Specimens

After specimen preparation, mechanical testing will proceed for both specimens, whether or not they have been dried. This is intended to ensure that the filament dryer can significantly

restore the filament's mechanical properties. The design of this test specimen was created in SolidWorks. Tests were carried out on two types of each specimen, including 1) tensile testing and 2) flexural testing. In accordance with ASTM (American Society for Testing and Materials) standards, each test uses a different specimen geometry: ASTM D638 for tensile testing [32] and ASTM D790 for flexural testing [33]. Specimens from each test type were checked three times to obtain a reliable estimate of the standard deviation. Figure 4 presents an overview of the tensile test specimen and the flexural test, in mm units, with a thickness of 3.2 mm.



(a) (b)

Figure 4. Testing specimen geometries in mm unit; a) tensile test, b) flexural test

Mechanical testing specimens were printed in three materials, PLA+, PETG, and ABS, on a BIQU B1 3D printer using parameter sets tuned to minimize warpage and maximize strength (see Table 2). After printing, three-point tensile and flexural properties were measured on a servo-hydraulic MTS testing system to capture the displacement profile against load, modulus, yield and ultimate strength, and strain/stress at break, with a suitable load cell at a force of 25/250 N-m, a load measurement accuracy of ±0.5%, and a stroke accuracy (crosshead speed) of ±0.1%. Dog-bone and rectangular flexural specimens were aligned with the loading axis, gripped to avoid slippage or crushing, and tested under displacement control. Furthermore, force–displacement data were recorded at high acquisition rates to compute the stress–strain curve. In addition, test speeds, span-to-depth ratios, and gauge lengths followed standard laboratory practice for polymer FFF parts, and at least three replicates per material–parameter set were evaluated to ensure statistical reliability. To provide clear details for replication, Table 3 presents the input parameters for the mechanical tensile and flexural tests.

Table 3. Input parameters in mechanical testing for tensile and flexural tests

Parameters	Value		Unit
	Tensile	Flexure	

Test Rate	0.2	0.1	mm/s
Span	-	51	mm
Strain End Point	-	10,000	mm/mm
Grip Separation	25	-	mm
Data Acquisition Rate	8	10	Hz
Adjusted Gage Length	57	-	mm
Specimen Width	13	12.7	mm
Specimen Thickness	3.2	3.2	mm

2.6. Optical Measurement through Scanning Electron Microscope

To examine the microstructural features governing water-absorption failure, the fracture surfaces were immediately examined with a JEOL JSM-IT210 Scanning Electron Microscope (SEM) after mechanical testing. Each fracture section was sectioned to expose a cross-section of the measuring region. Because the substrate is polymeric and susceptible to surface charging, specimens were coated with Pd to a thickness of 2 nm [34] on a 32 mm holder with a carbon tape cover, then loaded into the SEM. Imaging was performed at an accelerating voltage of 18 kV and a working distance of 9.4 mm in high-vacuum mode. Furthermore, detector selection (secondary electrons vs. backscattered electrons) was adjusted to emphasize topographic (ligament pull-out, river marks, voids) or compositional contrast (fillers, porosity edges). Global surveys were acquired at $100x$ to capture the overall fracture morphology and crack path. At the same time, higher-detail fields at $20000x$ were collected to address layer-to-layer fusion lines, inter-bead necks, and micro-void coalescence that control the integrity of the FFF part.

Before imaging, the microscope was calibrated using a certified pitch standard, and scale bars were embedded in all images and verified at the start of each session (see Table 4). For each material, at least five magnifications were imaged per specimen, and three specimens (PLA+, PETG, and ABS) per condition were evaluated. Image analysis included threshold-based segmentation and manual annotation to quantify interlayer bond widths and pore-size distributions. Moreover, beam current and dwell time were minimized to limit thermal damage. If localized charging was observed, the chamber pressure was switched to variable-pressure mode (30–60 Pa) and/or the stage was tilted by 5–10° to improve the signal without blurring the metrology. This SEM-based optical workflow provides reproducible, quantitative descriptors of fracture microstructure that are directly comparable across print parameters and drying conditions.

Table 4. Scanning Electron Microscope (SEM) calibration input

Parameters	Value	Unit

Accelerating voltage	18	kV
Scan time	40	s
Imaging size	1280 x 960	pixel
Working distance	9.4	mm
Dwell time	25600	ns
Surface magnification	100 – 20,000	-

2.7. Determination of Filament Water Content

Water adsorption on filaments can occur via contact with ambient air. Free air has a water content of 0.1– [35]. This suggests the possibility of water adsorption within the filament structure. Bhagia et al. [36] explained that water-moisture precipitation can occur when the filament reacts with water, breaks the chain, and reduces its mechanical properties. In addition, diffusion is an important process for absorbing water from the free air into the filaments [37]. The diffusion process shows the ability of water molecules to penetrate the material [38]. An illustration of the process is shown in Figure 5.

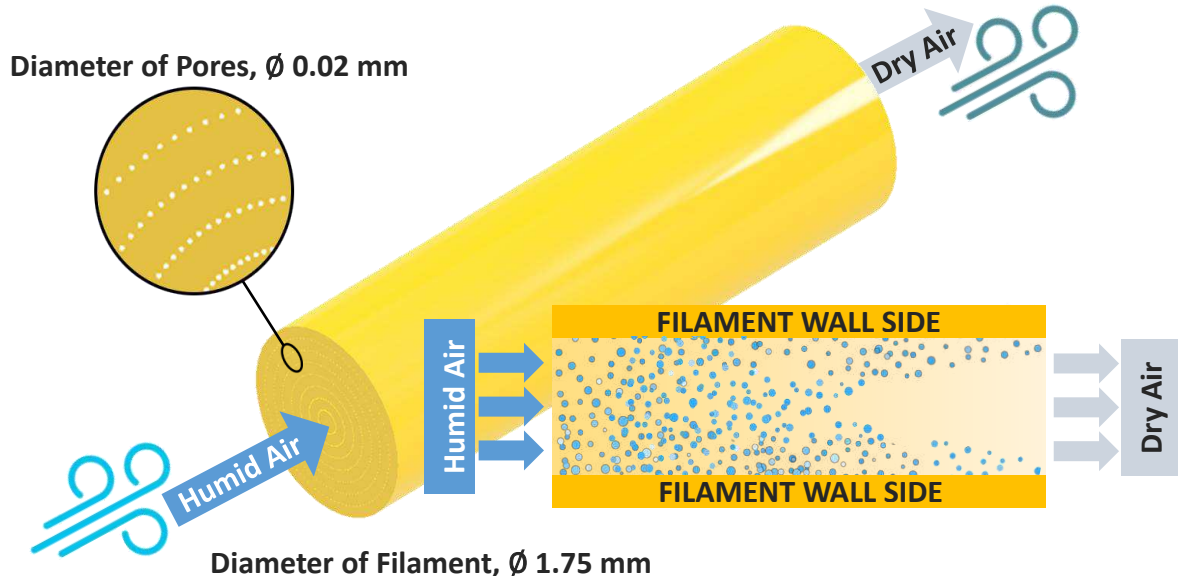


Figure 5. Schematic illustration of the hygroscopic process

To provide a clear theory of water diffusion, Adhikary et al. [39] determined the material diffusion coefficient (D), which can be formulated through equation (1).

$$D = \pi . \left(\frac{b . \theta}{4 . M_m} \right)^2 \quad (1)$$

Where b is the thickness of the composite (m); θ is the initial slope of a plot of $M(t)$ versus $t^{1/2}$; and M_m is the maximum weight gained (%). Thus, thermodynamic solubility (S) can be determined to generate the permeability (PM) presented in equations (2) and (3).

$$S = \frac{m_w}{m_{in}} \tag{2}$$

$$PM = D.S \tag{3}$$

m_w is the mass of adsorbed water in the equilibrium state and m_{in} is the initial mass of the material sheet.

In this study, the filaments were left in the open air for 1–4 weeks. For open-storage conditioning, spools are placed uncovered on a ventilated shelf under ambient laboratory conditions (22–25 °C, natural airflow, no direct fans) to avoid localized drying (see Figure 6). The coils are kept away from rain and water splashes and protected from direct sunlight and heat sources to prevent thermal softening. Exposure to dust is minimized by elevating them and wiping the surface weekly. We record weather events and avoid handling, except for inspection, to ensure consistent, real-world moisture absorption representative of typical workshop storage conditions.

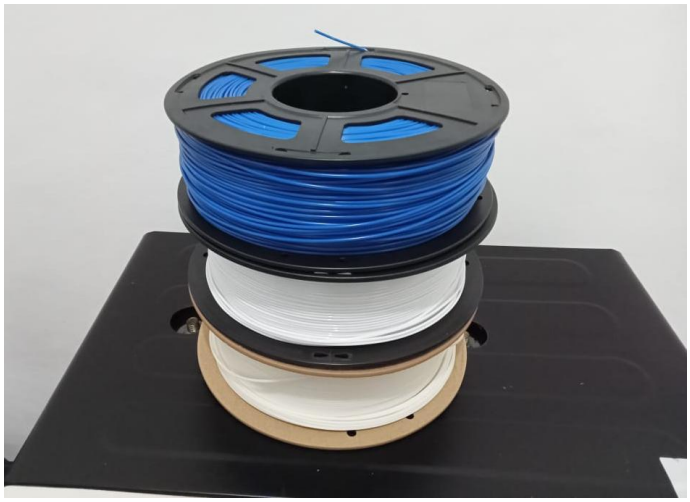


Figure 6. Filaments under an open storage condition

To quantify the water content trapped in the filaments, the filaments' weight was measured. The specimens used were PLA+, PETG, and ABS-based materials, which were formed into test specimens. This was intended to make the calculations in the test more consistent, thereby facilitating and improving the absorption and evaporation of moisture, as shown in Figure 7.



Figure 7. Test specimens for water absorption measurement

Guo et al. [40] also explained that moisture content can be determined using the following equation (4).

$$\text{Moisture content } (\%) = \frac{(\mathrm{W}_w - \mathrm{W}_d)}{\mathrm{W}_d}\, x\, 100 \qquad (4)$$

Where W_w represents the weight of the wet specimen (gr), and W_d represents the weight of the dry specimen (gr). Moisture content, expressed as a percentage, was measured for each of the three specimens.

2.8. Thermal Analysis and Heat Mapping

We measured heating dynamics by recording the rise in ambient temperature within the dryer's interior using embedded sensors positioned near the filament spools, shielded from direct radiation. In parallel, a FLIR infrared camera was used to map surface temperatures in predetermined regions for each filament type at scheduled points throughout the heating cycle. These IR images produced a spatially resolved heat field, allowing us to track how surface temperatures evolved relative to the dryer's ambient conditions.

After acquisition, the embedded sensor temperature and FLIR-derived temperature were synchronized over time and processed to generate a temperature-time curve. For each material, we plotted the minimum, maximum, and average surface. Therefore, a comparative plot of materials allows assessment of differences in thermal response.

To evaluate the model's fidelity, we performed transient thermal simulations in ANSYS using the ambient temperature history and the thermal profiles of each material from previous characterization as boundary conditions and calibration parameters in the simulation input. The simulated surface temperatures, shown as heat contours, were then compared with FLIR measurements at the corresponding timestamps. Eventually, we visualized side-by-side heat maps from the simulations and from the FLIR thermal camera to qualitatively assess spatial patterns and confirm the inferred heat-transfer mechanism.

2.9. Statistical Analysis Method

2.9.1. Specimen Size and Variance

The total specimen size (n = 108) used for both specimen weight and mechanical property analyses was derived from measurements collected over four consecutive weeks. These comprised pre-drying weeks 1-4, followed by a post-drying week, with specimens evaluated under three temperature treatments: 55 °C, 65 °C, and 75 °C. In each week, we collected n = 18 for weight and mechanical measurement, arising from three materials, including PLA+, PETG, and ABS. Within every material, specimens A – C were reserved for three-point flexural tests and specimens D – F for tensile strength tests (see Figure 8), yielding six observations per material in each week. For each specimen, we recorded its weight together with a complete set of mechanical properties (peak load, peak stress, stress at break, stress at yield, strain at break, and modulus). However, for the statistical analysis, only peak load, peak stress, and modulus were included because these variables had the fewest missing values. When separated by filament type, the mean specimen weights were 4.959 g (SD = 1.228) for PLA+, 6.647 g (SD = 1.495) for PETG, and 5.139 g (SD = 1.737) for ABS. For the retained mechanical properties, PLA+, PETG, and ABS showed mean peak loads of 619.144 N (SD = 555.776), 714.287 N (SD = 639.409), and 585.101 N (SD = 481.039), respectively; mean peak stresses of 43.528 MPa (SD = 18.924), 49.303 MPa (SD = 22.406), and 47.017 MPa (SD = 24.494); and mean moduli of 52.883 MPa (SD = 60.213), 52.584 MPa (SD = 58.503), and 49.874 MPa (SD = 51.801).

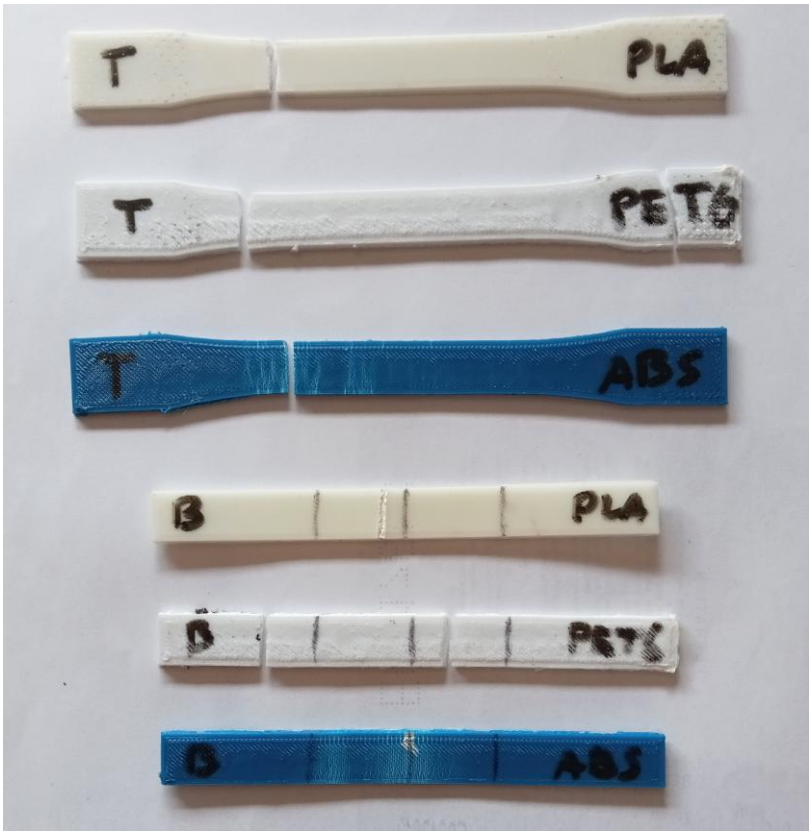


Figure 8. Printed specimens for mechanical testing, T = tensile, and B = bending (flexure)

A two-sided 95% confidence interval (α = 0.05) was adopted, using Z = 1.96. The standard error and margin of error were computed for each variable, and the minimum sample size was determined using the classical relation shown in Equation (5).

$$n = \left(\frac{Z\sigma}{ME}\right)^2 \tag{5}$$

as described in [41]. With ME specified as 5% of the mean, the required sample sizes were 94 for weight peak load, peak stress, and modulus.

2.9.2. Exploratory Data Analysis

Exploratory Data Analysis (EDA) is employed in this research as an essential process because it uses statistical and visualization techniques to explore datasets, reveal patterns, test hypotheses, and verify assumptions [42]. Basically, EDA helps in understanding the data structure before proceeding to hypothesis analysis. To assess the robustness and internal consistency of the experiment, we employed four complementary visualization approaches, including material-specific correlation heatmaps, specimen−material distribution plots, week-to-week trend charts, and per-metric boxplots by material. Together, these graphics offer a

multi-angle quality check on the data, supporting transparent evaluation of measurement reliability and experimental control without presupposing inferential outcomes.

2.9.3. Hypothesis Testing Framework

To assess between-material differences, we adopted a global-hypothesis framework rather than isolated pairwise tests, because simple pairwise t-tests are not appropriate when comparing three groups (PLA+, PETG, ABS) on each parameter and can inflate Type-I error. We first applied a one-way ANOVA with balanced groups, $n = 24$ for weight per material, respectively, as the primary test of H_0: μPLA+ = μPETG = μABS. Assumptions were checked a priori: Levene's test strongly rejected homogeneity of variances, and Shapiro–Wilk's test indicated non-normality. However, ANOVA was robust under these conditions of deviation with equal cell sizes, so we proceeded while also planning non-parametric confirmation. For validation, we ran the Kruskal–Wallis test, which also rejected the null with reasonableness standards including $H = 14.96$ and $p < 0.001$, confirming that at least one material was different. Post-hoc multiple comparisons were intended via Dunn's test, however, since such implementation was not available in our environment, we used the pairwise Mann–Whitney test with Bonferroni adjustment. This analysis pattern, including ANOVA, assumption checks, and non-parametric cross-checks with adjusted post-hoc, will provide converging evidence to reject H_0 Moreover, support material-level differences while controlling for family-wise error.

2.9.3.1. One-Way ANOVA and Assumption Diagnostics

The one-way ANOVA procedure operates under a parametric framework, in which each observation follows the model shown in Equation (6).

$$Y_{ij} = \mu + \tau_i + \varepsilon_{ij}, \tag{6}$$

where Y_{ij} represents the j-th observation within filament group i, μ represents the grand mean, τ_i represents the fixed material effect, and ε_{ij} represents residual error with parameter σ^2. Balanced group structure stabilized the estimate of σ^2 through symmetric sampling across groups. Diagnostic procedures evaluated the validity of model assumptions through formal tests of variance homogeneity and distributional form. The Levene statistic revealed strong evidence of diverging group variances, indicating that σ^2 does not remain constant across materials. The Shapiro–Wilk statistic revealed deviations from normal error distribution, indicating that ε_{ij} lacks ideal Gaussian behavior. Equal group sizes reduce the F-

statistic's sensitivity to such deviations, allowing continued use of the ANOVA model while acknowledging the necessity of confirmatory procedures. The resulting ANOVA outputs provided initial evidence for non-zero τ_i values, indicating parameter-level divergence among the filament groups.

2.9.3.2. Non-Parametric Validation

The Kruskal–Wallis procedure offered a distribution-free alternative for testing the equality of location parameters across groups. The corresponding null hypothesis states that the distributional medians $M_{\mathrm{PLA+}}, M_{\mathrm{PETG}}, M_{\mathrm{ABS}}$ remain equal across materials. The test statistic, based on rank-sum differences, decisively rejected this equality, yielding parameter-level confirmation of the ANOVA findings under minimal distributional assumptions. Post-hoc evaluation employed the Mann–Whitney procedure with Bonferroni-adjusted significance thresholds. The adjustment introduced strict control over the family-wise error rate, preserving the validity of parameter inference across multiple contrasts. The overall structure of this validation layer produced inferential convergence between parametric mean-based testing and nonparametric median-based testing, thereby enhancing the credibility of all detected group differences.

2.9.3.3. Multivariate Analysis of Variance (MANOVA) with Blocking Factor

The MANOVA framework expanded the analysis to a multivariate response vector provided in Equation (7).

$$\mathrm{Y} = [\text{Weight, PeakLoad, PeakStress, Modulus}] \tag{7}$$

with each component treated as a correlated parameter set influenced by filament type, drying stage, and specimen identity. The multivariate linear model took the form of Equation (8).

$$\mathrm{Y}_{ijk} = \mu + \alpha_i + \beta_j + \gamma_k + \varepsilon_{ijk}, \tag{8}$$

where μ denotes the vector of grand means, α_i denotes the filament effect vector, β_j denotes the temporal effect vector, γ_k denotes the specimen blocking vector, and ε_{ijk} denotes the multivariate error vector with covariance matrix Σ. The Wilks' Λ statistics revealed substantial differences across the parameter vectors α_i and β_j, with an interaction effect that indicated divergent temporal trajectories among filaments. The blocking variable produced extreme significance, indicating that the parameters γ_k captured a large portion of inherent specimen

variability, a property frequently observed in additive manufacturing environments. The MANOVA structure provided a comprehensive parameter-level assessment of the mechanical system, with results reflecting the joint behavior of multiple correlated outputs rather than isolated univariate responses.

3. Results and Discussion

3.1. Modification of Filament Dryer

The filament dryer design incorporates heater control elements to improve the performance of the 3D-printing filament-drying process. The control elements consist of an Omron MY2-P6DY PT100 as the temperature sensor, an Omron E5CC as the main controller, and an Omron CN101A as the programmable timer. Both control elements are integrated into the filament dryer to ensure that drying conditions comply with environmental and filament standards. This is important to note because, when using a conventional oven, the drying temperature cannot be automatically adjusted to the standard temperature, and the available drying time is very limited (maximum 1 hour). By adding a control element, the temperature and time parameters can be adjusted in accordance with industry standards (approximately 55–85°C over 3–6 hours) to improve filament properties. The results of the development and modification of the filament dryer by adding electronic components are shown in Figures 9 and 10. To ensure that the components function properly, tests were conducted at several points as follows.



Figure 9. Modified filament dryer

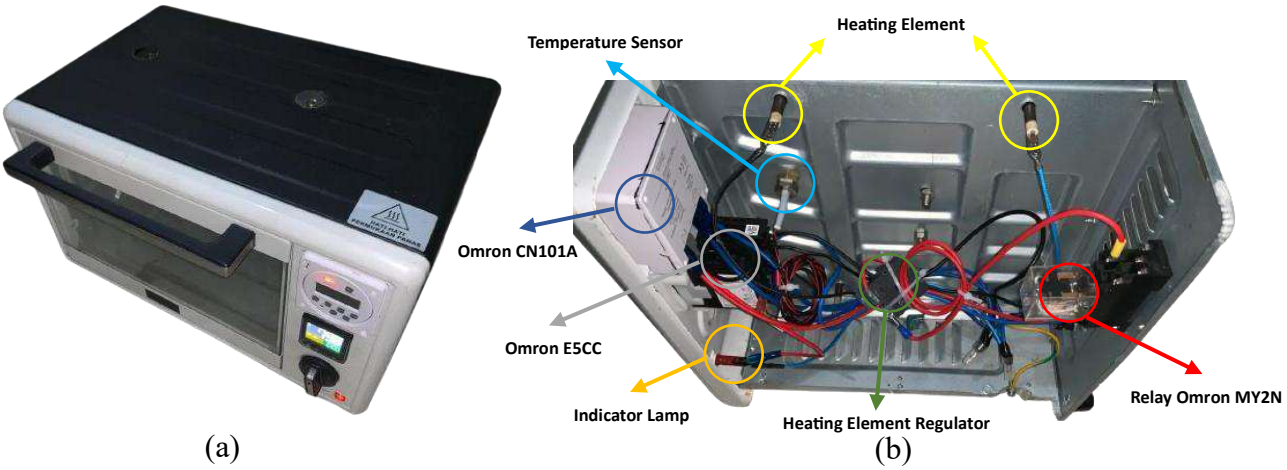
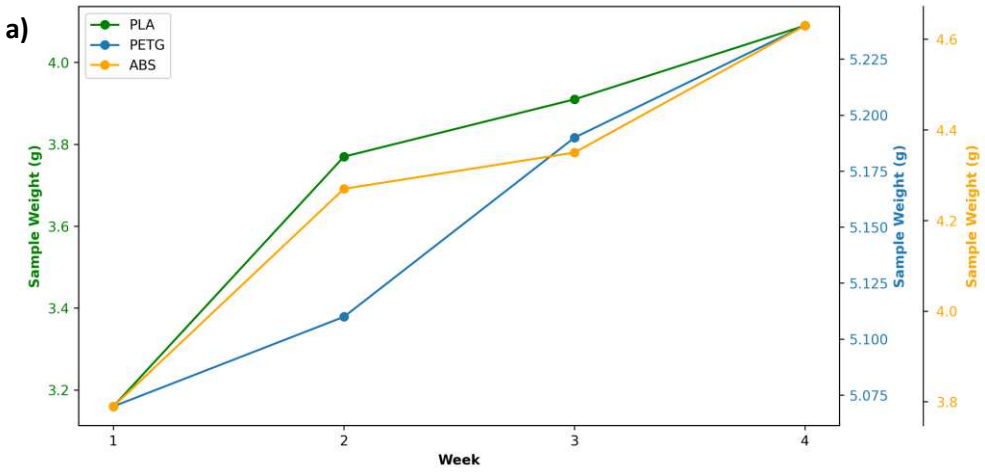


Figure 10. Filament dryer modification results: a) outside view and b) inside view

3.2. Moisture Uptake During Open Storage

The unsealed filaments were immediately printed into mechanical test specimens. Each specimen was weighed to determine its initial mass before being stored under open-air conditions. To simulate degradation during use, the filament spools were stored for four weeks. Each week, moisture content is determined by weighing the specimen and calculating the difference between its current weight and the previous week's weight. The trend is evident in Figure 11 and Table 5.



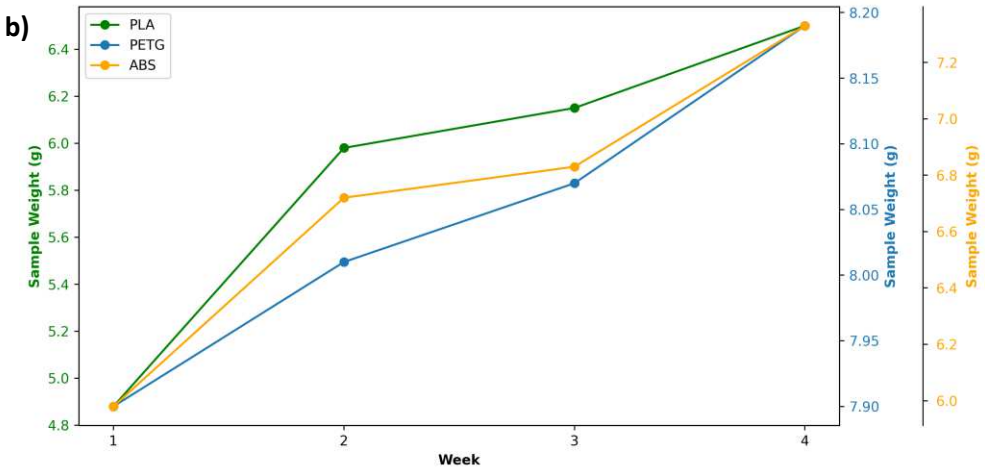


Figure 11. Trend of increasing specimens' weight over several weeks in different testing, a) flexure, b) tensile

Table 5. Open storage moisture content measurement

Storage Periods	Current Weight			Moisture Content (%)		
	PLA+	PETG	ABS	PLA+	PETG	ABS
Flexure						
Week 1	3.16	5.07	3.79	0.00	0.00	0.00
Week 2	3.77	5.11	4.27	19.30	0.79	12.66
Week 3	3.91	5.19	4.35	23.73	2.37	14.78
Week 4	4.09	5.24	4.63	29.43	3.35	22.16
Tensile						
Week 1	4.88	7.9	5.98	0.00	0.00	0.00
Week 2	5.98	8.01	6.72	22.54	1.39	12.37
Week 3	6.15	8.07	6.83	26.02	2.15	14.21
Week 4	6.5	8.19	7.33	33.20	3.67	22.58

Based on Table 5, the filaments had water content after being left in the open air for four weeks. Under open storage conditions, the filament's water content consistently increased (see Figure 15). This increase occurred in weeks 1, 2, 3, and 4, where PLA+ showed the highest moisture uptake, with a sharp rise in water content from week 1 to week 4 for both flexural and tensile specimens, indicating that this material is the most sensitive to ambient humidity due to its hygroscopic properties [45]. ABS also absorbed a noticeable amount of moisture, but its values remained lower than PLA+ [46], placing it in an intermediate position. By contrast, PETG exhibited the lowest water absorption throughout the storage period, with only a slight increase in moisture content over time, confirming that PETG is the least affected by open-air storage and even slight fluctuation in ambient temperature among the three filaments [47].

Based on the gravimetric analysis, the results for testing new filaments for up to four weeks are consistent with Mitch Walleser's theory, as reported by Aniskevich et al. [48], which explains that filaments exhibit hygroscopic properties that increase specimen weight due to moisture absorption from highly saturated ambient air.

3.3. Mechanical Degradation After Moisture Aging

The 3D printing filaments, left in open air for 1 – 4 weeks, were then further processed through mechanical testing, including flexural and tensile tests, to determine the effect of air-water absorption on their mechanical strength. Mechanical testing was performed three times per test (two tests) for each material (three materials), yielding 18 specimens, with testing conducted once per week. Furthermore, Figures 12 and 13 present the results of mechanical testing of 3D-printing filaments after four weeks of open storage.

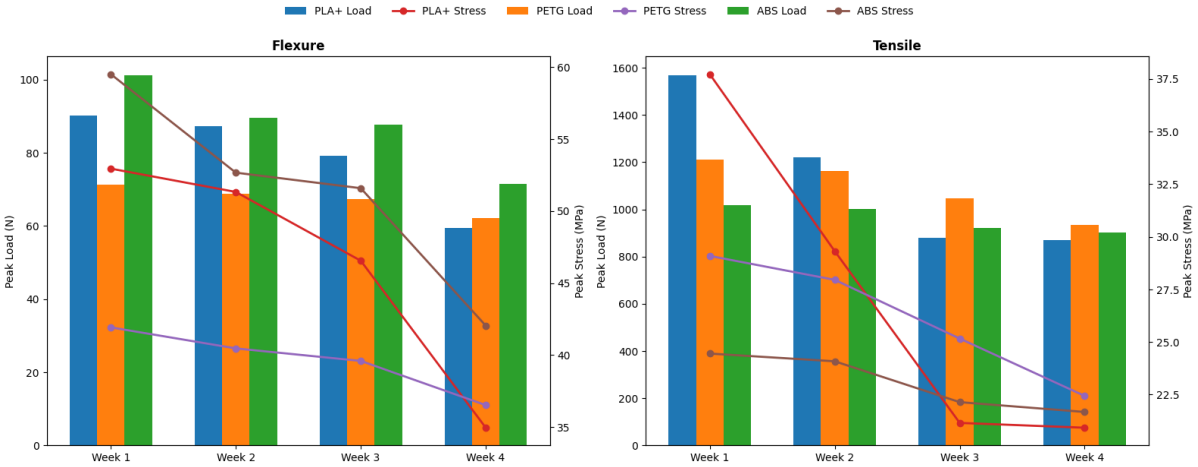


Figure 12. Trend of mechanical properties (peak load and peak stress) in both flexural test and tensile test, where bars and lines indicate peak load and peak stress, respectively

Based on Figure 12, the longer the 3D printing filament is stored in open air, the greater the moisture it traps, which progressively degrades its mechanical integrity, reducing the peak load and peak stress over the 4-week open-air storage period. As water diffuses into the material, it acts as a plasticizer within the polymer matrix and at filament interfaces, weakening intermolecular interactions and reducing effective load transfer across the printed layers [49]. This degradation is most pronounced in PLA+ and, to a lesser extent, ABS, which exhibit the steepest reductions in both peak load and peak stress, consistent with their higher measured moisture uptake [50]. In contrast, PETG retains a greater fraction of its initial mechanical performance and shows the smallest decline in peak load and stress, in line with its lower water absorption, indicating a

comparatively higher resistance of its microstructure to environmental exposure due to its high degree of crystallinity [51].

To further clarify the filament's capabilities under applied loads, Figure 12 shows the load-displacement curves for the three materials in the first and fourth weeks of open storage, as shown in Figure 13. In the flexural test, the week-1 curves show that ABS attains the highest peak load and the most significant displacement at failure, closely followed by PLA+. In contrast, PETG reaches a lower peak load and fails at a smaller displacement, with a sharp post-peak drop that reflects more brittle flexural behavior and lower energy absorption [52] [53]. After four weeks, all three materials exhibit reduced peak loads and much shorter displacements, and the curves terminate more abruptly, indicating a clear loss of flexural strength and ductility.

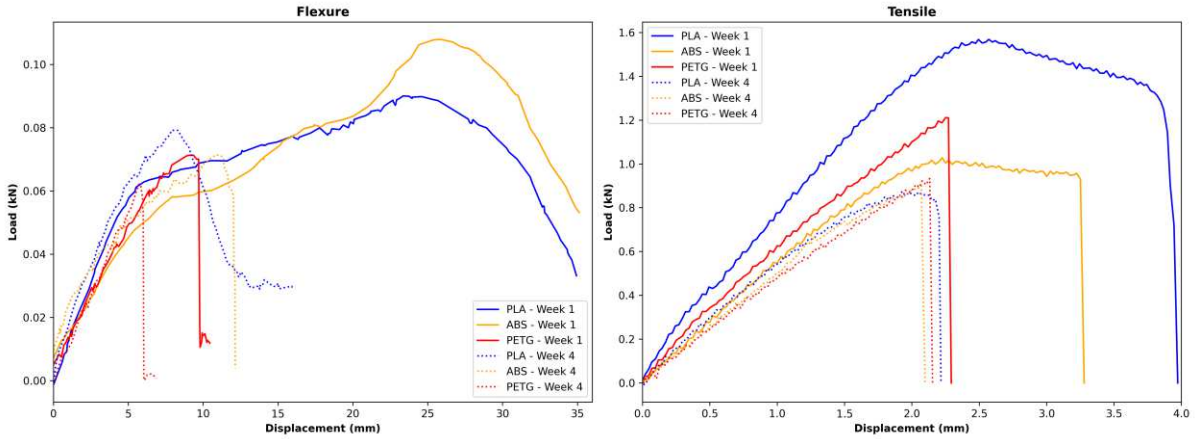


Figure 13. Load and displacement curves on each specimen in open storage for the first and fourth weeks before drying treatment

On the other hand, tensile loading in week-1 PLA+ yields the highest load and exhibits the most significant displacement before fracture. This behavior was confirmed by D'Andrea et al. [54], who explained that PLA+ had the highest mechanical properties at 0° orientation, followed by ABS and PETG. By week 4, the curves for all filaments shift downward and end at smaller displacements, confirming that prolonged open-air storage to ambient humidity reduces both tensile strength and elongation at break [55]. Overall, these curves indicate that the filaments performed well in both flexural and tensile tests. However, their load-bearing capacity and ductility decreased significantly after four weeks of exposure.

3.4. Optimization Results Based on Filament Drying Process

To mitigate the decrease in filament strength after four weeks of open storage, a drying process is required to remove water and restore mechanical properties, thereby increasing the

material's strength. Until the drying process was carried out at the temperature variations tested for five hours, the three filaments were printed again using a 3D printer to form a model whose mechanical properties would be re-tested to determine the comparison between the fourth week open-storage filaments and the filaments that had been dried using the modified filament dryer discussed previously. These results are further summarized in Table 6.

Table 6. Peak stress (MPa) comparison of specimens before and after drying

Filaments	Before Drying (Week 4)		Treatment Temperature	Duration	After Drying	
	Flexure	Tensile			Flexure	Tensile
PLA+	34.95	20.929	55	5 hours	68.3	33.95
			65		68.6	28.8
			75		65.05	29.9
PETG	36.52	22.44	55	5 hours	80.5	40.9
			65		96.9	40.55
			75		75.9	40.8
ABS	42.04	21.677	55	5 hours	61.45	22.4
			65		72.95	27.95
			75		81.25	29.05

Table 6 shows that drying the filaments for five hours markedly increased both flexural and tensile stresses across all materials. For each filament, the mechanical values after drying were consistently higher than those before drying, with each filament achieving its best condition. Stress (flexural and tensile) was highest at 55 °C, 65 °C, and 75 °C for PLA+, PETG, and ABS, respectively. 3DTrcek Industry confirmed the results [56], which emphasized that PLA+ reaches its optimum drying at 55 °C and that drying above 60 °C should be avoided due to its relatively low glass transition temperature (Tg) [57]. Moreover, Siraya Tech confirmed that the recommended drying temperature for PETG is 65 °C8], consistent with its slightly higher Tg and greater thermal stability compared to PLA+ [59]. In addition, Anycubic clarified that the optimal drying temperature for ABS filament is 75 °C [60], which aligns with ABS's higher Tg and its ability to withstand more aggressive thermal treatment without distortion [61]. Collectively, these external recommendations align well with the experimental results, supporting the conclusion that each filament type requires a distinct, material-specific drying temperature to maximize mechanical performance while avoiding thermal degradation.

After drying, PETG exhibits the highest absolute values of flexural and tensile strength [62]. Meanwhile, ABS generally maintains the next-highest flexural strength but the lowest tensile strength, as noted by Dundar et al., who reported that the compressive strength of ABS is approximately 20% higher than its tensile strength [63]. Moreover, PLA+ lies between them in both loading modes. The effect of temperature is pronounced for both flexural and tensile

properties [65], with substantial recovery already achieved at 55 °C, and further increasing the temperature to 65 °C yields additional gains, particularly for PETG and ABS, indicating that 55 °C is sufficient to remove most of the moisture from the filaments. However, to optimize conditions for each filament, an appropriate temperature is still required to achieve the highest mechanical properties (see Table 6).

As additional results, we further visualize the beneficial effects of filament drying after 4 weeks of open storage using load-displacement and stress-strain curves (see Figure 14). Overall, the dried specimens show a substantial recovery in mechanical performance, with higher initial slopes, increased peak loads, and larger areas under the curves. This recovery is evident in all three materials, reversing the plasticizing effect of absorbed water and partially healing interfacial defects.

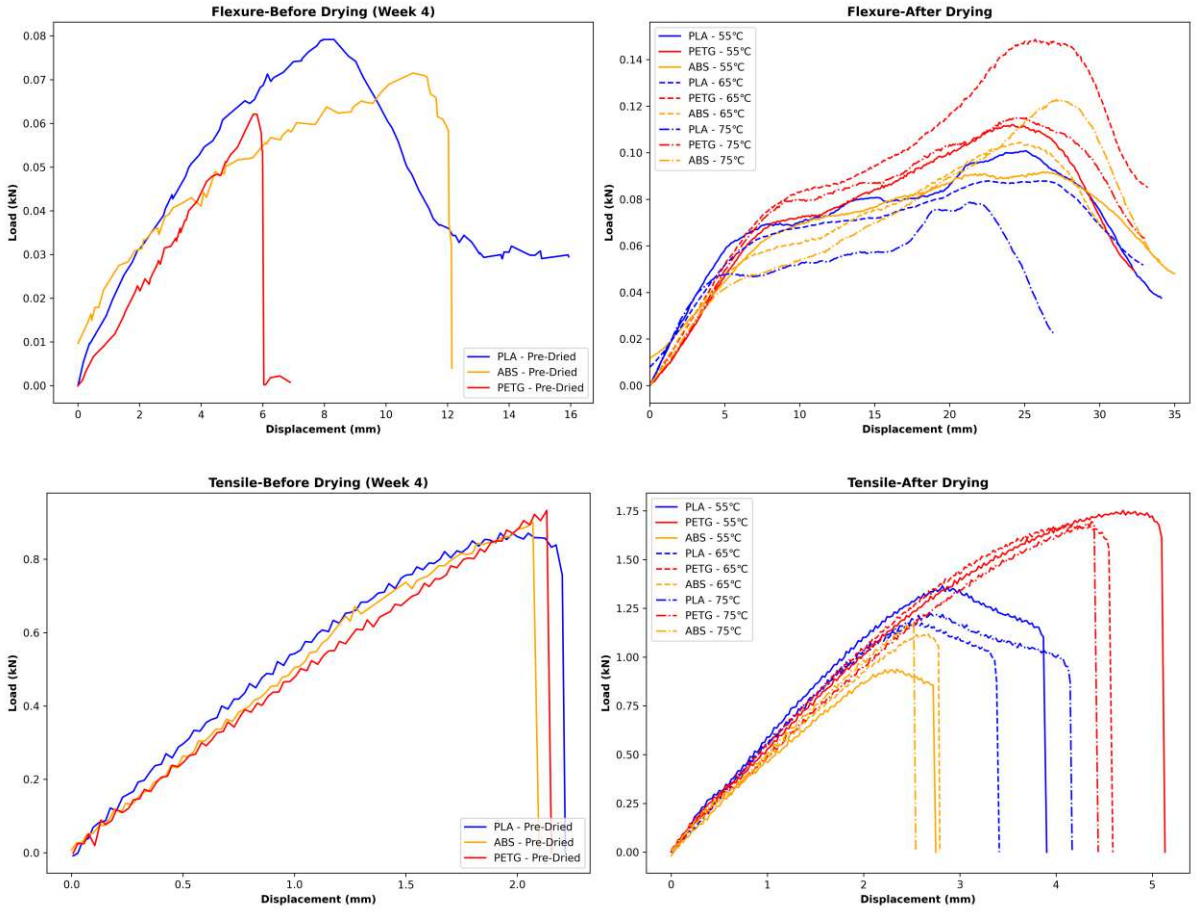


Figure 14. Mechanical curves on each specimen test, before and after drying treatment

The mechanical trends are consistent with the microstructural features observed in SEM analysis of the specimens (see Figure 15). In the fourth week, non-dried samples, the fracture surfaces reveal pronounced interlayer gaps, microvoids, and crack propagation along the bead

boundaries, confirming that moisture ingress promotes interfacial decohesion and weakens load transfer. By contrast, the first-week specimens exhibit relatively smooth surfaces with well-fused filaments, in line with their higher peak load and displacement. After the drying treatment, the specimens show a marked reduction in open voids and crack density, with tighter interlayer contact and a more cohesive fracture path, indicating recovery of interfacial bonding. This microstructural healing is consistent with the restored load-displacement response, demonstrating that thermal drying mitigates moisture-induced damage and re-establishes the structural integrity of the printed filaments.

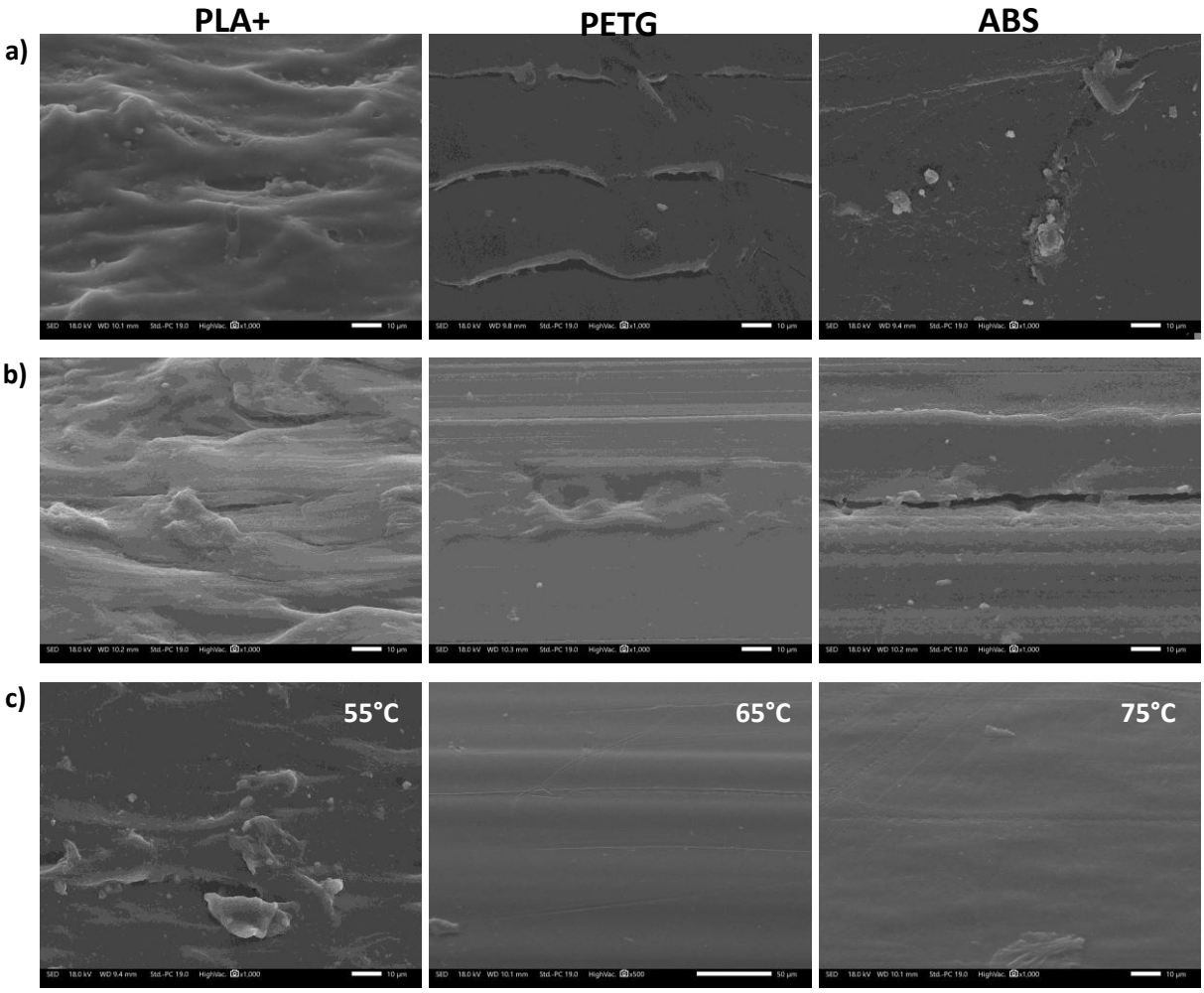


Figure 15. SEM visualization of filaments under certain conditions; a) first week, b) fourth week undried, c) dried at the best temperature

Overall, these results demonstrate that an appropriate thermal drying protocol can effectively restore, and in some cases closely approach, the original mechanical properties of FFF filaments following prolonged exposure to ambient humidity. Thus, a suitable combination of temperature and duration is required to maintain the material's strength. This is supported

by research by Andreozzi et al. [66], who found that dried filaments increase the material's strength relative to undried filaments.

3.5. Comparison of Surface Appearance

The trends in mechanical performance and SEM observations are further clarified by the macroscopic surface appearance of the printed parts (see Figure 16). Specimens printed directly from humid filament exhibit rough, matt surfaces with visible stringing, blobbing, and irregular bead contours, particularly in overhanging regions. These defects are consistent with moisture-induced foaming during extrusion [64], in which entrapped water rapidly vaporizes at the hot end, generating bubbles that disrupt melt flow and reduce dimensional fidelity. The resulting porosity and unstable filament deposition are consistent with the increased interlayer voids and crack propagation observed in the fourth-week SEM images, as well as with the reduced peak load and stiffness measured in both flexural and tensile tests.

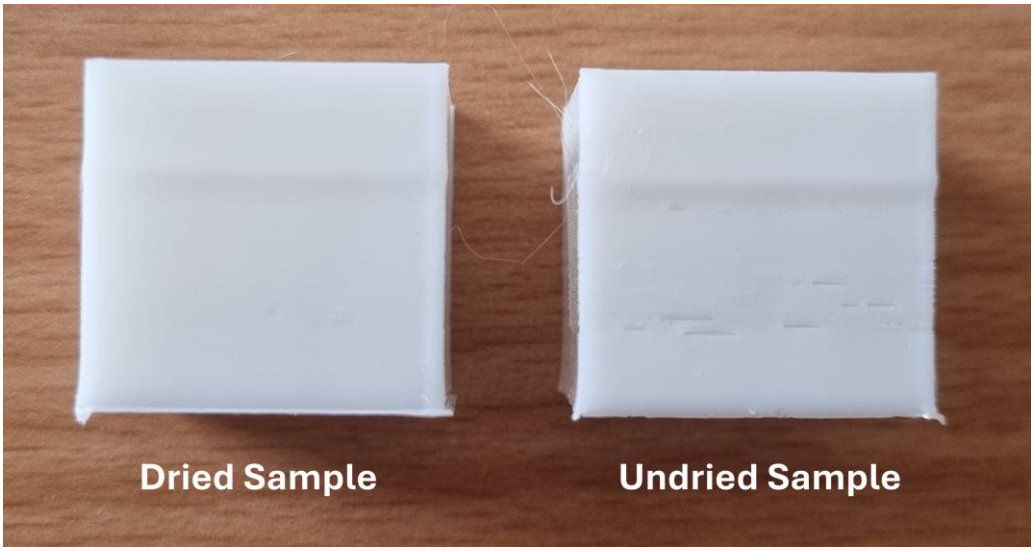


Figure 16. Macroscopic appearance of dried and undried filaments on printed objects

By contrast, prints produced from filaments subjected to the drying protocol exhibited significantly smoother, more homogeneous surfaces due to improved polymer-matrix bonding [65]. The improved surface quality indicates a more stable extrusion flow from the 3D printer, supporting the microstructural evidence of reduced void content and improved interfacial bonding after drying. This visual recovery of surface quality paralleled the mechanical recovery observed in the load-displacement curves and SEM analysis, confirming that removing absorbed moisture not only restored the overall mechanical properties but also improved the

aesthetic and dimensional quality of the FFF parts, thereby supporting improved 3D printing performance.

3.6. Thermal Evidence and Numerical Transient Simulation

The transient simulation begins by measuring the filament-drying temperature profile over time. This experimentally obtained profile is crucial because it captures the time-dependent boundary conditions for the drying process. This data was then imported into ANSYS transient thermal simulation to model heat transfer, yielding temperature contour plots for each filament type. The ultimate validation step involves a direct comparison of the simulated temperature contours with the actual heat profiles and contours captured by a thermal camera at the corresponding temperature points, yielding an absolute difference of 9.63% (see Figure 17).

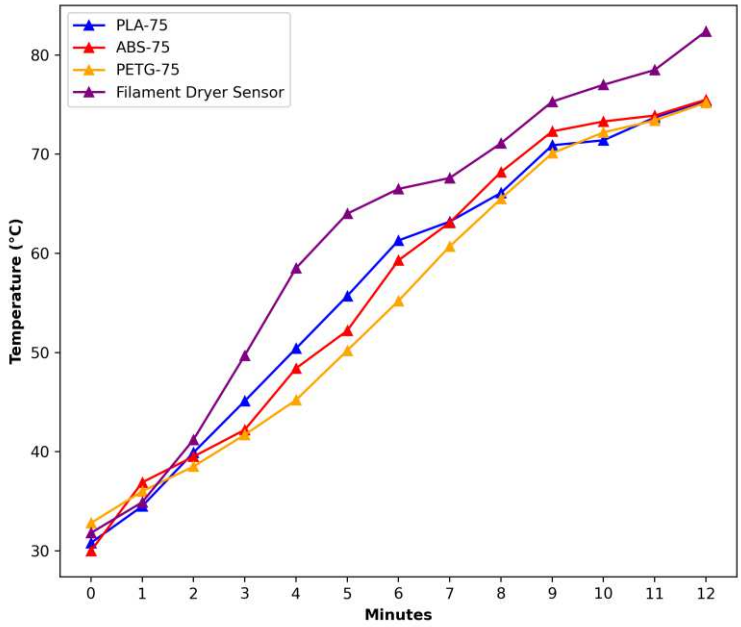


Figure 17. Temperature sensor profile toward the experimental heat behavior of each filament every minute

Figure 17 shows the heating profiles of the three filaments compared with the filament dryer's internal sensor during drying at 75 °C. All curves begin near room temperature (30–32 °C) and increase steadily with time. Generally, the dryer sensor consistently records a significant increase in temperature, indicating that the air inside the dryer heats up faster than the filament cores. PLA+ shows the highest heating rate, reaching about 70 – 75 °C by 9 – 10 minutes, while PETG and ABS follow closely behind, which warms slightly more slowly and remains a few degrees cooler than PLA+ throughout most of the cycle, suggesting that PETG and ABS have higher glass transition (Tg) temperature and other thermal properties than PLA+

[66]. By the end of the 12 minutes, all three materials converge toward the target temperature, indicating a brief thermal lag between the dryer environment and the actual filament temperature.

Building on the transient thermal profile derived from the filament dryer data in Figure 17 and implemented as a time-dependent boundary condition in ANSYS, the simulation was extended to predict the temperature distribution within the actual specimen geometry (a dogbone for tensile testing) for each material and drying temperature (see Figure 18). Note that this configuration has the same effect as the flexural test specimen.

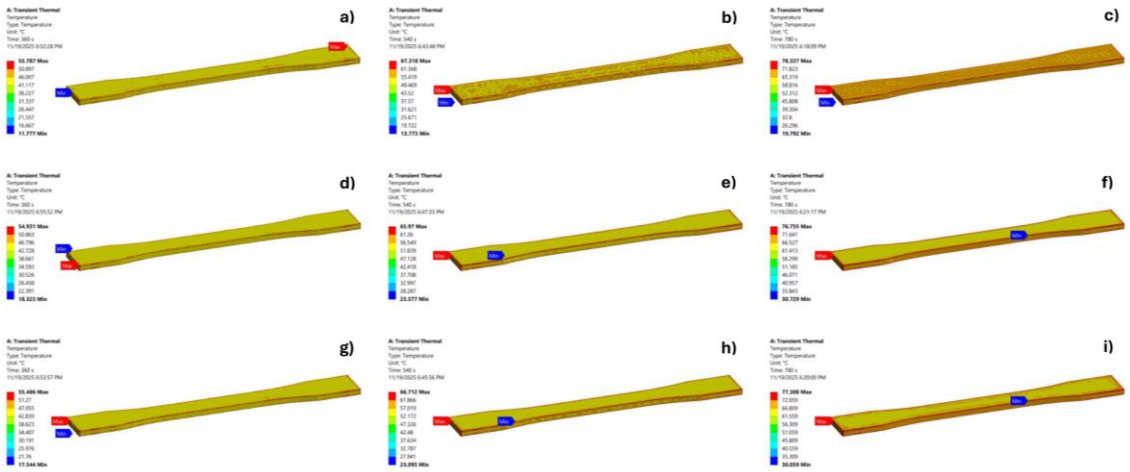


Figure 18. Simulated thermal contour of specimen temperatures; PLA+ at temperature of a) 55 °C, b) 65 °C, c) 75 °C; PETG at temperature of d) 55 °C, e) 65 °C, f) 75 °C; and ABS at temperature of g) 55 °C, h) 65 °C, i) 75 °C

In all cases, the temperature field along the gauge section is relatively uniform, confirming that the specimens rapidly approach the imposed ambient temperature profile, with only small gradients localized near the clamped end and the thicker transition region. By applying the same heating history to PLA+, PETG, and ABS at 55, 65, and 75 °C, the average specimen temperature rises accordingly, and the residual cold zones diminish, revealing how rapidly and effectively heat penetrates the filament during drying. Minor differences among materials are visible, with PLA+ and ABS showing slightly steeper thermal gradients than PETG. Overall, the numerical results verify that the applied drying conditions are sufficient to raise the entire specimen to the target temperature, providing a basis for linking filament drying conditions to the thermal simulation of the samples.

To validate the accuracy of the transient thermal model and the predicted temperature contours in Figure 18, the numerical results were subsequently compared with the experimental

thermal distributions at their peak temperatures, as measured with a FLIR infrared camera (see Figure 19). By matching the characteristic peak-temperature patterns between finite-element (FE) contours and thermal camera images at target set points, the method can assess how well the simulation captures the system's actual heating behavior.

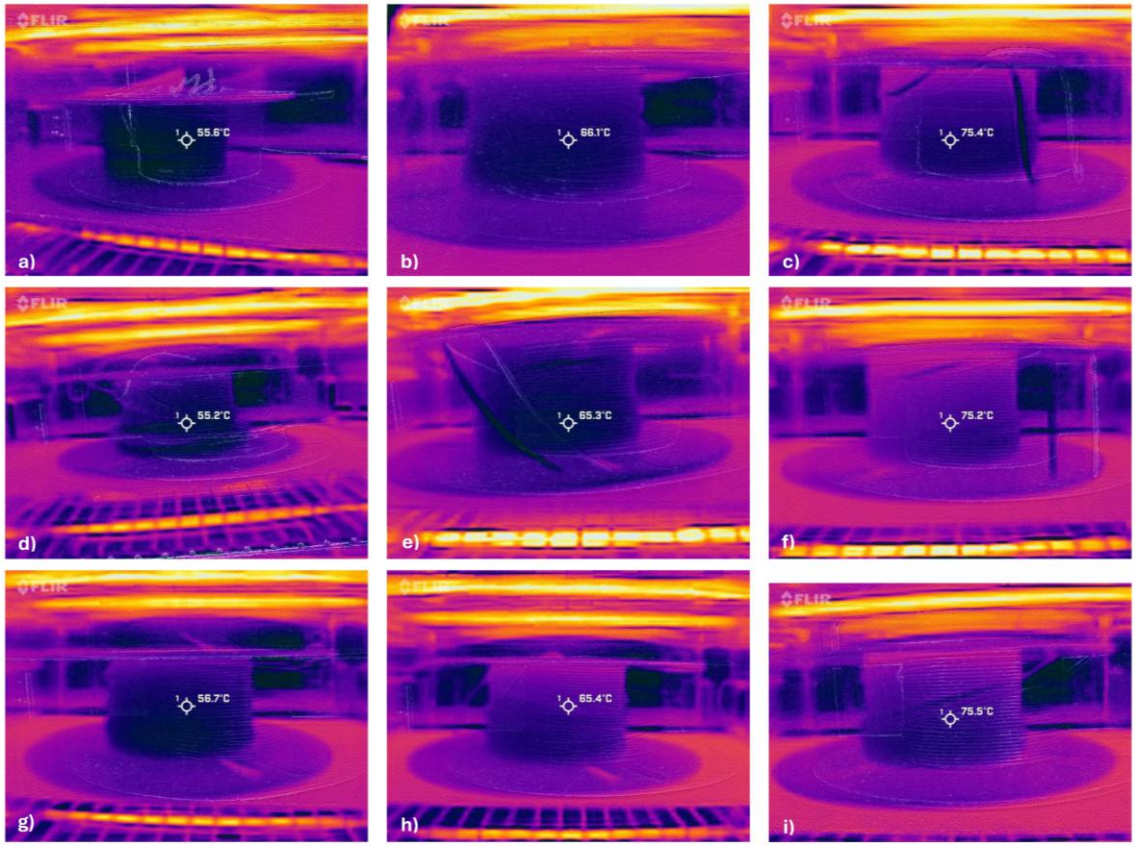


Figure 19. Thermal distribution of filaments in experimental imaging; PLA+ at temperature of a) 55 °C, b) 65 °C, c) 75 °C; PETG at temperature of d) 55 °C, e) 65 °C, f) 75 °C; and ABS at temperature of g) 55 °C, h) 65 °C, i) 75 °C

Taken together, Figures 17–19 demonstrate that the heating process and the thermal models are highly accurate and mutually consistent. The time–temperature curves in Figure 21 show only a slight lag relative to the dryer's internal sensor, whereas the simulated temperature contours in Figure 22 predict nearly uniform temperature fields along the flexural specimens for PLA+, PETG, and ABS at 55, 65, and 75 °C, with only slight end-to-end gradients. The infrared images closely match these predictions in Figure 23, where the measured surface temperatures of the filament spool cluster tightly cluster around the target values and exhibit similar spatial distributions. The close agreement between sensor readings, numerical simulations, and experimental thermal images confirms the accuracy of the thermal model and

the reliability of the filament dryer in reaching and maintaining the prescribed drying temperatures.

3.7. Multivariate Interpretation of Recovery Behavior

3.7.1. Descriptive Statistics

As mentioned in the methods section, the statistical analysis is divided into weight measurements and mechanical properties. For the specimen size, the initial power calculation indicated that a minimum of 94 samples were required to achieve a 95% confidence level with a maximum allowable error of 5%, respectively. Therefore, 108 (weight and mechanical properties) specimens were prepared and measured to exceed this requirement. As summarized in Table 7, the weight measurements produced a mean of 4.959 g with a standard deviation of 1.228, reflecting moderate variability in specimen mass. Mechanical properties (peak load (PL), peak stress (PS), and modulus (M)) had mean values of 619.144 N, 43.528 MPa, and 52.883 MPa, with corresponding standard deviations of 555.776, 18.924, and 60.213. The greater dispersion of these mechanical parameters relative to weight is consistent with expectations for polymeric materials, as mechanical responses are inherently more sensitive to filament-specific microstructural characteristics and stress–strain behavior.

Table 7. Specimen size for pre-statistical analysis

Filament	Variable	Mean ($\bar{x}$)	SD (s)	SEM	95% CI ($\alpha = 0.05$)
PLA+	Weight (g)	4.959	1.228	0.1182	[4.728, 5.190]
	Peak Load (N)	619.144	555.776	53.443	[514.399, 723.889]
	Peak Stress (MPa)	43.528	18.924	1.822	[39.957, 47.099]
	Modulus (MPa)	52.883	60.213	5.797	[41.523, 64.243]
PETG	Weight (g)	6.647	1.495	0.1438	[6.365, 6.929]
	Peak Load (N)	714.287	639.409	61.514	[593.721, 834.853]
	Peak Stress (MPa)	49.303	22.406	2.155	[45.082, 53.524]
	Modulus (MPa)	52.584	58.503	5.629	[41.551, 63.617]
ABS	Weight (g)	5.139	1.737	0.1672	[4.811, 5.467]
	Peak Load (N)	585.101	481.039	46.277	[494.397, 675.805]
	Peak Stress (MPa)	47.017	24.494	2.358	[42.396, 51.638]
	Modulus (MPa)	49.874	51.801	4.985	[40.103, 59.645]

The 95% confidence intervals reported in Table 7 demonstrate that the estimated population means for each filament fall within well-bounded ranges across all measured variables. For weight, the intervals span 4.73–5.19 g for PLA+, 6.37–6.93 g for PETG, and 4.81–5.47 g for ABS, indicating precise and consistent mass measurements within each material category. Moreover, a relatively narrow range for the population mean ($\bar{x}$) commonly

described as high precision, which indicates that the collected data is reliable and specific [54]. Similarly, the confidence intervals for mechanical properties (peak load, peak stress, and modulus) capture the expected material-specific variability while remaining sufficiently narrow to support reliable inference. These bounded intervals, together with the relatively small measurement standard errors (SEM), reflect high measurement precision and confirm the dataset's stability. Collectively, these metrics affirm that the chosen specimen size (n = 108 per filament) provides statistically robust estimates of both weight and mechanical responses, ensuring that subsequent analyses are well supported by adequate statistical power.

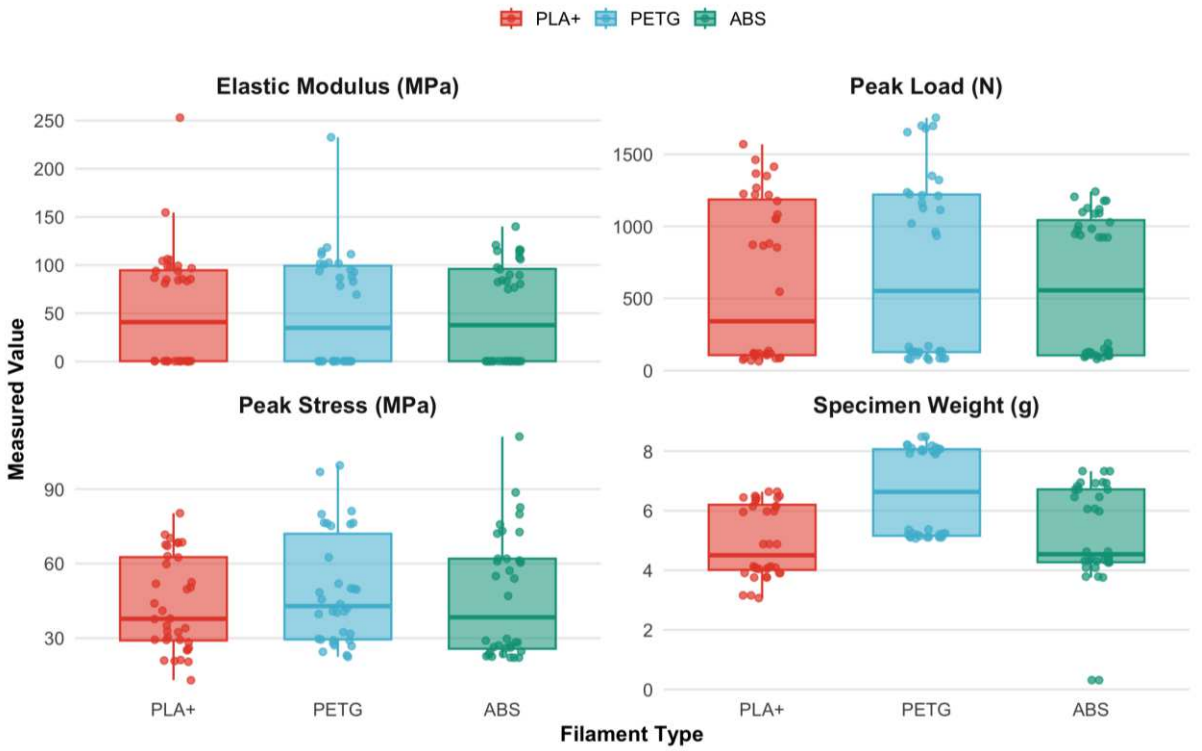


Figure 20. Mechanical Properties by Filament Type

To analyze dataset characteristics and investigate hidden patterns and relationships, the Exploratory Data Analysis (EDA) is performed as a bridge before uncovering the data for subsequent modeling and hypothesis testing [55]. The EDA stage serves to interrogate the structure of the measurements, assess variability within and across filaments, and evaluate whether the data conform to expected mechanical behaviors. As part of this process, Figure 24 provides a visual summary of the distributional characteristics of elastic modulus, peak load, peak stress, and specimen weight for PLA+, PETG, and ABS. The combination of boxplots and overlaid raw observations allows simultaneous inspection of central tendency, dispersion,

and outlier behavior, thereby facilitating a more nuanced understanding of material-level differences.

The graphical patterns observed in Figure 20 reinforce the numerical trends presented in Table 7. ABS consistently exhibits higher stiffness and reduced variability in elastic modulus, reflecting its characteristic rigidity and stable mechanical response. PETG exhibits a broader range of peak load and stress values, consistent with its ductile nature and greater sensitivity to local structural irregularities, whereas PLA+ shows lower medians and wider spreads, indicating a stronger dependence on processing conditions. The specimen weight distributions further differentiate the materials, with PETG forming a clearly higher mass cluster and PLA+ and ABS occupying overlapping but more compact ranges. These visual distinctions confirm that each filament possesses a distinct mechanical signature, supporting the premise that filament type is a primary source of variation in the dataset.

3.7.2. Multivariate Analysis

Building directly on the descriptive and exploratory findings, a multivariate inferential analysis was conducted to formally evaluate whether weight and mechanical properties vary collectively as a function of drying stage (Time), filament type, and specimen identity. While univariate summaries and boxplots provide valuable preliminary insight, they cannot fully capture the interdependence among weight, peak load, peak stress, and modulus, variables that are inherently correlated due to shared material and structural determinants. As such, a Multivariate Analysis of Variance (MANOVA) was employed to test simultaneous differences across these response variables while accounting for the repeated-measures structure by including specimen as a blocking factor. The full MANOVA output is provided in Table 8.

Table 8. MANOVA Results for Combined Mechanical Responses

	df	**Wilks**	***p-value***
Time	6	0.292	< .000***
Filament	2	0.345	< .000***
Specimen	23	0.005	< .000***
Time: Filament	12	0.335	0.015*
Residuals	62		

Note: *Signif. codes: 0 ***' 0.001 '**' 0.01 '*' 0.05 '.' 0.1'' 1*

The MANOVA results identify four statistically meaningful effects. First, the drying stage exhibits a substantial multivariate impact (Wilks' $\Lambda = 0.29185$, $F = 3.6521$, $p = 1.939 \times 10^{-7}$ (< .000)), indicating that the transition from Pre-drying conditions to various Post-drying temperatures produces coordinated shifts across all measured responses. This confirms that

drying acts as a multidimensional transformation rather than affecting weight or mechanical behavior independently.

Second, filament type significantly differentiates the combined response vector (Wilks' $\Lambda = 0.34569$, $F = 10.3371$, $p = 6.999 \times 10^{-11}$ (< .000)). This finding is consistent with patterns noted earlier in the EDA; however, the multivariate test demonstrates that material distinctions extend well beyond individual metrics and encompass the complete mechanical profile. These systematic differences reflect fundamental variations in polymer chemistry, morphology, and thermal stability.

Third, the block effect for specimen identity is highly significant (Wilks' $\Lambda = 0.00597$, $F = 6.7895$, $p < 2.2 \times 10^{-16}$ (<.000)), highlighting considerable baseline variability among specimens. This variability aligns with the specimen-resolved distribution patterns shown in Figure 21 and supports explicitly modeling specimen ID. Incorporating this factor prevents confounding between intrinsic specimen variation and treatment effects.

Finally, the interaction between drying stage and filament is statistically significant (Wilks' $\Lambda = 0.33476$, $F = 1.5696$, $p = 0.01577$). This demonstrates that each filament follows a distinct mechanical evolution as drying progresses. PLA+ shows a gradual increase in stiffness, PETG displays an early rise followed by stabilization, and ABS exhibits a nonlinear trajectory influenced by relaxation and embrittlement. This interaction underscores the necessity of multivariate modeling, as such material-specific temporal paths cannot be fully captured through independent univariate analyses.

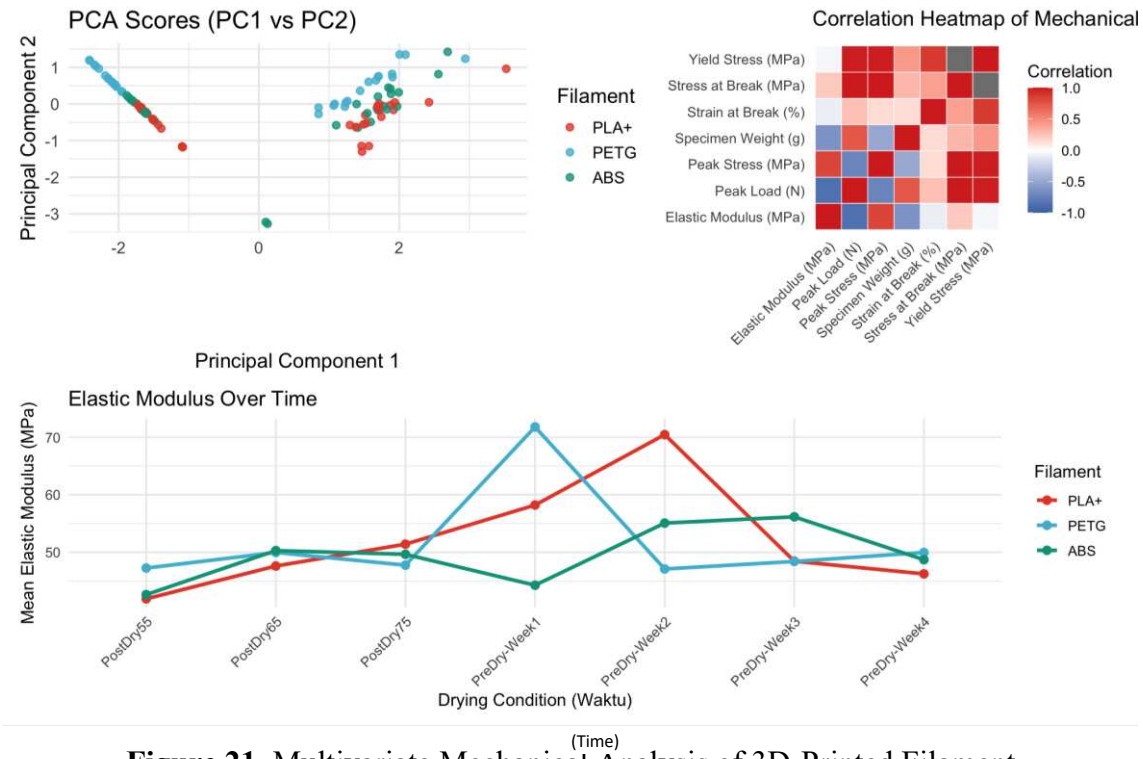


Figure 21. Multivariate Mechanical Analysis of 3D-Printed Filament

To visualize these multivariate relationships, PCA was applied (see Figure 22). The score plot shows clear separation between filaments, with PC1 (79% variance) dominated by stiffness-related variables and PC2 (13% variance) associated with weight. PLA+ forms a compact cluster, indicating consistent mechanical responses; PETG shows broader variation, reflecting differences in weight and strain-related behavior; and ABS occupies a distinct high-stiffness region. The PCA score plot (PC1 vs. PC2) demonstrates clear separation among filament types, indicating that their overall mechanical behavior differs systematically when all mechanical properties are considered simultaneously. PC1, which captures the largest share of total variance, is strongly associated with stiffness-related variables such as Peak Load, Peak Stress, and Elastic Modulus, whereas PC2 reflects contributions from mass- and failure-related properties, particularly Specimen Weight and Strain at Break. This separation implies that even when individual metrics show partial overlap, the combined mechanical signature of each filament is distinct.

PLA+ forms a relatively compact cluster in PCA space, suggesting more homogeneous mechanical performance across drying stages. PETG shows greater spread along PC2, indicating greater variability in strain-related behaviors and mass distribution across specimens. ABS forms the most distinct cluster, separating primarily along PC1. This is consistent with ABS's inherently different failure mechanics and stiffness compared with PLA+ and PETG, reflecting its lower modulus and other responses to thermal histories. The clustering

pattern also suggests that ABS is more sensitive to changes in its internal microstructure during the drying process, whereas PLA+ exhibits more stable behavior.

The correlation heatmap highlights strong internal coherence among most strength-related variables. Peak Load, Peak Stress, and Elastic Modulus exhibit strong positive correlations, indicating that stiffer specimens tend to withstand higher loads. Conversely, Strain at Break shows inverse correlations with stiffness parameters, suggesting that stiffer materials tend to exhibit lower ductility. Specimen Weight displays only modest correlations with strength metrics, implying that dimensional or density variations do not directly predict mechanical performance in these materials.

The temporal trend in Elastic Modulus across drying conditions further clarifies how each filament responds to moisture reduction and thermal exposure. PLA+ exhibits a moderate increase in modulus from post-dry conditions to pre-drying week 2, suggesting that controlled moisture reduction improves stiffness by stabilizing internal polymer chains. PETG shows a sharper rise and subsequent stabilization, indicating a drying-induced stiffening effect that peaks earlier in the sequence. ABS presents a comparatively nonlinear pattern, with modulus increasing substantially in pre-drying week 2 before decreasing slightly thereafter. This behavior aligns with ABS's known sensitivity to microstructural relaxation processes, in which drying initially increases stiffness but prolonged exposure may cause internal stress redistribution or mild embrittlement.

Collectively, these results indicate that both filament type and drying condition (time) exert significant multivariate effects on mechanical performance. The MANOVA results support this, showing highly substantial effects for Filament, Time (drying stage), and their interaction. The significant Time × Filament interaction reveals that each material's mechanical trajectory over time is unique. PLA+ and PETG tend to stiffen during drying, whereas ABS exhibits more complex behavior, influenced by both stiffening and relaxation mechanisms. The strong significance of the Specimen factor further confirms the presence of intrinsic variability across printed units, underscoring the importance of treating specimen identity as a blocking variable in multivariate models.

Overall, these combined analyses demonstrate that the mechanical properties of 3D-printed polymers cannot be fully understood using a single metric. Instead, multivariate techniques such as PCA and MANOVA reveal deeper structural patterns, capture the interplay among stiffness, strength, ductility, and mass, and clarify how environmental conditioning differentially shapes the mechanical profiles of PLA+, PETG, and ABS. These insights have

direct implications for optimizing filament selection, print parameters, and drying protocols in engineering applications requiring predictable material behavior.

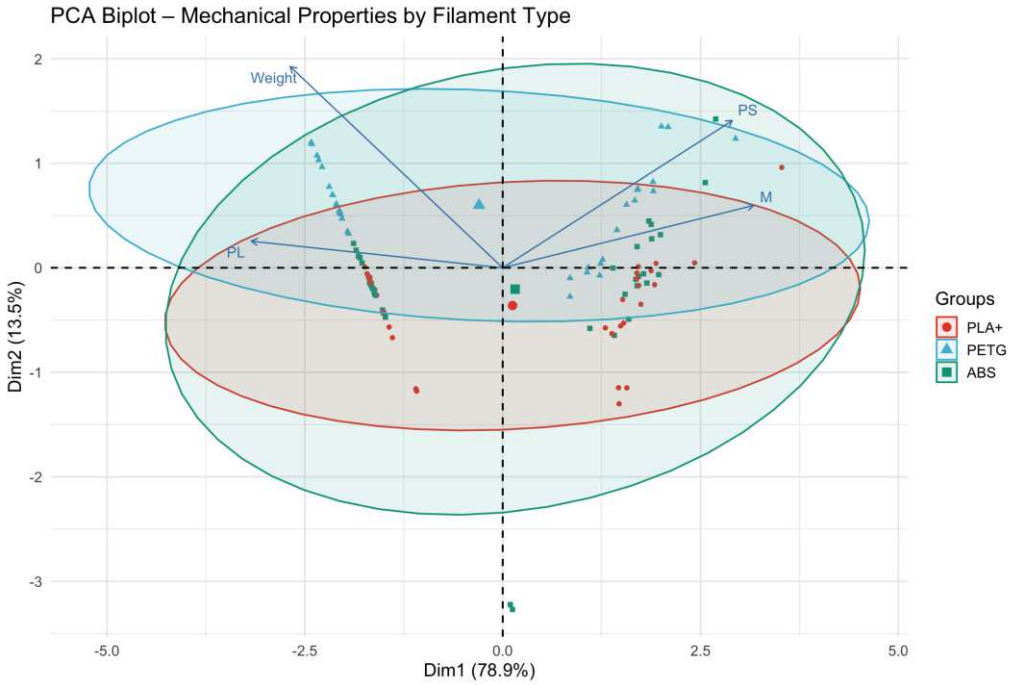


Figure 22. PCA Biplot

The PCA biplot reveals distinct multivariate mechanical behavior among the three filament types (PLA+, PETG, and ABS). Principal Component 1 (PC1), which accounts for 78.9% of the variance, is strongly associated with Peak Stress (PS), Elastic Modulus (M), and Peak Load (PL), indicating that this component primarily reflects overall stiffness and load-bearing capacity. Materials positioned further to the right along PC1 therefore, exhibit higher mechanical strength. Principal Component 2 (PC2), accounting for 13.5% of the variance, is primarily influenced by Specimen Weight, suggesting that mass-related differences contribute to secondary variation across specimens. The orientation and length of the variable arrows show that PS and M are the dominant contributors to group separation. At the same time, Weight contributes orthogonally, reflecting an independent source of variability.

The group ellipses highlight clear clustering patterns. PETG specimens occupy a region characterized by higher PC2 values, indicating relatively greater variation in weight and stress-related features. ABS forms a broader ellipse, stretching across the PC1 axis, consistent with its more variable modulus and stress responses. In contrast, PLA+ clusters more tightly, reflecting greater mechanical consistency across drying conditions. The relative separation of the ellipses demonstrates that each filament has a distinct multivariate signature, with minimal

overlap among groups. Additionally, the PS and M vectors pointing to the right indicate that ABS and PETG tend to exhibit higher combined stiffness and stress tolerance than PLA+, whereas PLA+ appears more centrally located, with moderate values of these properties.

Moreover, the PCA biplot shows that the mechanical behavior of the 3D-printed polymers emerges from the combined influence of stiffness, load-bearing capacity, and mass characteristics, and that these interacting dimensions clearly distinguish the filament types within the multivariate response space. This, in turn, corroborates the MANOVA findings, underscoring filament type as a statistically significant determinant of the specimens' integrated mechanical performance.

3.8. Industrial Implications and Adoptions

Building on the strong agreement between our experimental results and manufacturer-recommended drying temperatures, the present findings have both theoretical and practical implications for the industrial adoption of FFF filaments. Theoretically, the work clarifies the coupled effects of moisture uptake, storage time, and material-specific drying temperature on the mechanical response of PLA+, PETG, and ABS, providing quantitative relationships between water content, peak stress, and displacement behavior that can feed into predictive models, design rules, and future standards for filament conditioning. In practice, the identified optimal curing conditions (55 °C for PLA+, 65 °C for PETG, and 75 °C for ABS) for five hours were adapted into a simple, low-cost protocol that can be implemented in existing printing facilities and production lines to recover and stabilize mechanical properties after exposure to ambient temperatures.

While these findings already offer clear, actionable guidance for industrial drying and handling of FFF filaments, we also highlight important avenues for future research. A key limitation of the present work is the simple gravimetric approach used to estimate moisture content during the 4-week open-storage period, where water uptake was inferred solely from bulk mass change. This method cannot resolve spatial moisture gradients within the filament, is sensitive to minor weighing errors and surface contamination, and does not capture real-time sorption–desorption kinetics under fluctuating ambient conditions. In future studies, we will employ more advanced characterization tools, such as dynamic vapor sorption (DVS), to monitor continuous mass change under controlled temperature and humidity, as demonstrated by Zou et al. [67], and complement this with Karl Fischer titration for accurate absolute water-content calibration. Such instrumentation would provide higher-resolution data, enabling more

rigorous coupled moisture–mechanical models and further refining the practical drying and storage protocols.

Beyond these methodological limitations, another consideration is that this work does not fully represent the range of competing perspectives within the broader FFF community and the literature. Our discussion focuses on studies and manufacturer guidelines that support the importance of drying and identify optimal temperatures for PLA+, PETG, and ABS. In contrast, this study did not compare alternative conditioning strategies, such as in-line filament dryers, closed desiccant dry boxes, or direct printing from dry storage. However, some practitioners consider these to be superior to batch drying. Therefore, future work should systematically combine and test these contrasting approaches and perspectives from both academic studies and industrial practice to provide a more balanced assessment of the importance of filament drying and of strategies that account for cost, complexity, and mechanical performance.

By applying an optimized drying process to reduce filament moisture, manufacturers can restore the performance of previously exposed spools while retaining several important advantages. Lower moisture levels reduce print defects and failed jobs, which, in turn, minimize scrap and unnecessary reprints. At the same time, controlled pre-drying stabilizes tensile and flexural properties along the spool, resulting in more predictable and reliable mechanical behavior. Because the drying protocol can be standardized as a repeatable pre-process step, printer setup becomes faster and less dependent on operator trial-and-error. Crucially, the ability to recover moisture-exposed spools also supports circularity programs, enabling reclaimed filaments to be reused rather than discarded, thereby improving cost efficiency and environmental impact.

4. Conclusions

The existing oven was modified by embedding control elements, enabling precise temperature regulation and drying time control. With this upgraded control, the drying cycle can be set to industry-relevant conditions, effectively removing moisture from 3D-printing filaments and improving their mechanical performance. Tests at different temperatures showed that filaments left exposed for four weeks could be restored and, in many cases, exceed their original strength after drying. In practice, the optimal drying conditions, 55 °C for PLA+, 65 °C for PETG, and 75 °C for ABS for five hours, form a simple, low-cost protocol that can be readily implemented in existing printing facilities. Under these conditions, peak flexural stress for PLA+, PETG, and ABS increased from 34.95, 36.52, and 42.04 MPa to 68.3, 96.9, and

81.25 MPa, respectively. In contrast, tensile peak stress rose from 20.92, 22.44, and 21.67 MPa to 33.95, 40.55, and 29.05 MPa, confirming substantial recovery of material properties. This improvement was supported by analyses of load-displacement curves, SEM imaging of fracture surfaces, and macroscopic surface comparisons before and after drying, which collectively indicate improved 3D printing performance. In addition, the close agreement between temperature sensor readings, numerical simulations, and thermal imaging validates the accuracy of the thermal model and the reliability of the filament dryer in reaching and maintaining the prescribed drying temperatures. Multivariate analyses (MANOVA and PCA) verified that the optimized drying conditions produced statistically significant improvements across all mechanical responses ($Wilks_{filament} = 0.345, p_{filament} < .000, Wilks_{time} = 0.292, p_{time} < .000, Wilks_{interaction} = 0.335, p_{interaction} = .015$). PCA further demonstrated clear group separation, with PC1 explaining 79% of the variance and dominated by stiffness-related variables; PETG showed the greatest post-drying shift, indicating the best multivariate recovery. At the same time, all filaments exhibited statistically robust enhancement in overall mechanical performance.

Funding

This research was supported by institutional research funding. Detailed funding information will be provided after the double-blind review process.

Conflict of interest

The authors declare that they have no conflict of interest.

Data Availability

The data that support the findings of this study are available from the corresponding author upon reasonable request.

Author Contributions

All authors contributed to the study conception and design. Material preparation, data collection, experimental testing, and data analysis were performed collaboratively by the authors. All authors contributed to manuscript drafting, revision, and final approval of the submitted version.

References

[1] M. Moradi *et al.*, "Correlation between Infill Percentages, Layer Width, and Mechanical Properties in Fused Deposition Modelling of Poly-Lactic Acid 3D Printing," *Machines 2023, Vol. 11, Page 950*, vol. 11, no. 10, p. 950, Oct. 2023, doi: 10.3390/MACHINES11100950.

[2] Y. L. Chan *et al.*, "Review on 3D Printing Filaments Used in Fused Deposition Modeling Method for Dermatological Preparations," *Molecules 2025, Vol. 30, Page 2411*, vol. 30, no. 11, p. 2411, May 2025, doi: 10.3390/MOLECULES30112411.

[3] P. Gkertzos, A. Kotzakolios, G. Mantzouranis, and V. Kostopoulos, "Nozzle temperature calibration in 3D printing," *International Journal on Interactive Design and Manufacturing (IJIDeM) 2023 18:2*, vol. 18, no. 2, pp. 879–899, Dec. 2023, doi: 10.1007/S12008-023-01681-2.

[4] S. A. M. Tofail, E. P. Koumoulos, A. Bandyopadhyay, S. Bose, L. O'Donoghue, and C. Charitidis, "Additive manufacturing: scientific and technological challenges, market uptake and opportunities," *Materials Today*, vol. 21, no. 1, pp. 22–37, Jan. 2018, doi: 10.1016/J.MATTOD.2017.07.001.

[5] A. Mecheter, F. Tarlochan, and M. Kucukvar, "A Review of Conventional versus Additive Manufacturing for Metals: Life-Cycle Environmental and Economic Analysis," *Sustainability 2023, Vol. 15, Page 12299*, vol. 15, no. 16, p. 12299, Aug. 2023, doi: 10.3390/SU151612299.

[6] Y. Wu and G. Chiu, "An Improved Height Difference Based Model of Height Profile for Drop-on-Demand 3D Printing with UV Curable Ink," *Proceedings of the American Control Conference*, vol. 2021-May, pp. 491–495, May 2021, doi: 10.23919/ACC50511.2021.9483241.

[7] O. Mehrabi, S. M. Hossein Seyedkashi, and M. Moradi, "Experimental and response surface study on additive manufacturing of functionally graded steel-inconel wall using direct laser metal deposition," *Opt Laser Technol*, vol. 167, p. 109707, Dec. 2023, doi: 10.1016/J.OPTLASTEC.2023.109707.

[8] L. Lendvai, I. Fekete, S. K. Jakab, G. Szarka, K. Verebélyi, and B. Iván, "Influence of environmental humidity during filament storage on the structural and mechanical properties of material extrusion 3D-printed poly(lactic acid) parts," *Results in Engineering*, vol. 24, p. 103013, Dec. 2024, doi: 10.1016/J.RINENG.2024.103013.

[9] E. Rezvani Ghomi *et al.*, "The Life Cycle Assessment for Polylactic Acid (PLA) to Make It a Low-Carbon Material," *Polymers (Basel)*, vol. 13, no. 11, p. 1854, Jun. 2021, doi: 10.3390/POLYM13111854.

[10] S. Olivera, H. B. Muralidhara, K. Venkatesh, K. Gopalakrishna, and C. S. Vivek, "Plating on acrylonitrile–butadiene–styrene (ABS) plastic: a review," *Journal of Materials Science 2016 51:8*, vol. 51, no. 8, pp. 3657–3674, Jan. 2016, doi: 10.1007/S10853-015-9668-7.

[11] O. Tunçel, Ç. Kahya, and K. Tüfekci, "Optimization of Flexural Performance of PETG Samples Produced by Fused Filament Fabrication with Response Surface Method," *Polymers 2024, Vol. 16, Page 2020*, vol. 16, no. 14, p. 2020, Jul. 2024, doi: 10.3390/POLYM16142020.

[12] S. Prajapati, J. K. Sharma, S. Kumar, S. Pandey, and M. K. Pandey, "A review on comparison of physical and mechanical properties of PLA, ABS, TPU, and PETG

manufactured engineering components by using fused deposition modelling," *Mater Today Proc*, May 2024, doi: 10.1016/J.MATPR.2024.05.018.

[13] M. Balasrinivasan, A. Varun Kumar, and K. Sathickbasha, "A comparative study on mechanical properties of PLA, PETG, and carbon fiber prepared by fused deposition modeling," *Proceedings of the Institution of Mechanical Engineers, Part E: Journal of Process Mechanical Engineering*, 2024, doi: 10.1177/09544089241301961;PAGE:STRING:ARTICLE/CHAPTER.

[14] B. Eyri, O. Gul, S. Yilmaz, N. G. Karsli, and T. Yilmaz, "Characterization of ABS/PETG multi-material composites 3D printed by print-pause-print method," *Polym Eng Sci*, vol. 65, no. 5, pp. 2353–2369, May 2025, doi: 10.1002/PEN.27151;PAGE:STRING:ARTICLE/CHAPTER.

[15] A. Saldaña-Robles, A. Sánchez-Angeles, A. de J. Balvantín-García, D. A. Núñez-Altamirano, and G. Capilla-González, "Mechanical behavior of 3D printed polymers under tensile and bending loads," *Advances in Science and Technology. Research Journal*, vol. 19, no. 10, pp. 371–384, 2025, doi: 10.12913/22998624/207989.

[16] R. A. Hamid, F. H. Hamezah, and J. Abd Razak, "Influence of Humidity on the Tensile Strength of 3D Printed PLA Filament," *Lecture Notes in Mechanical Engineering*, vol. 25, pp. 497–502, 2022, doi: 10.1007/978-981-16-8954-3_47.

[17] B. Singaravel, T. Niranjan, P. Laxmireddy, K. Srinivasulu, B. Chakradhar, and G. Poojitha, "Experimental investigation of degradation in the marine environment of FDM-based 3D printed specimens," *International Journal of Lightweight Materials and Manufacture*, Aug. 2025, doi: 10.1016/J.IJLMM.2025.08.002.

[18] Y. Huang, M. C. Leu, J. Mazumder, and A. Donmez, "Additive manufacturing: Current state, future potential, gaps and needs, and recommendations," *Journal of Manufacturing Science and Engineering, Transactions of the ASME*, vol. 137, no. 1, Feb. 2015, doi: 10.1115/1.4028725/375256.

[19] A. D. Banjo, V. Agrawal, M. L. Auad, and A. D. N. Celestine, "Moisture-induced changes in the mechanical behavior of 3D printed polymers," *Composites Part C: Open Access*, vol. 7, p. 100243, Mar. 2022, doi: 10.1016/J.JCOMC.2022.100243.

[20] H. Gong, M. Runzi, Z. Wang, L. Wu, and Y. Zhang, "Influence of Filament Moisture on 3D Printing Nylon," *Technologies 2025, Vol. 13, Page 376*, vol. 13, no. 8, p. 376, Aug. 2025, doi: 10.3390/TECHNOLOGIES13080376.

[21] M. Andreozzi *et al.*, "Effect of moisture content on the mechanical performance of 3D printed continuous reinforced two-matrix composite," *The International Journal of Advanced Manufacturing Technology 2024 133:11*, vol. 133, no. 11, pp. 5117–5126, Jun. 2024, doi: 10.1007/S00170-024-14041-5.

[22] Y. Cui, S. Gao, R. Zhang, L. Cheng, and J. Yu, "Study on the Moisture Absorption and Thermal Properties of Hygroscopic Exothermic Fibers and Related Interactions with Water Molecules," *Polymers 2020, Vol. 12, Page 98*, vol. 12, no. 1, p. 98, Jan. 2020, doi: 10.3390/POLYM12010098.

[23] P. Lertsarawut, S. Laksee, T. Rattanawongwiboon, and K. Hemvichian, "Eco-friendly alginate-starch-based water super-absorbent beads spherically shaped and uniformly fabricated via spherification and radiation-assisted polymerization," *Carbohydrate Polymer Technologies and Applications*, vol. 7, p. 100456, Jun. 2024, doi: 10.1016/J.CARPTA.2024.100456.

[24] F. Comino, P. E. Romero, E. Molero, and M. Ruiz de Adana, “Experimental evaluation of a 3D printed air dehumidification system developed with green desiccant materials,” *Appl Therm Eng*, vol. 227, p. 120393, Jun. 2023, doi: 10.1016/J.APPLTHERMALENG.2023.120393.

[25] M. Rafat *et al.*, “Assessment of Beaded, Powdered and Coated Desiccants for Atmospheric Water Harvesting in Arid Environments,” *Environments 2025, Vol. 12, Page 110*, vol. 12, no. 4, p. 110, Apr. 2025, doi: 10.3390/ENVIRONMENTS12040110.

[26] J. J. Słowiński, M. Roszak, M. Kazimierczak, G. Skrzypczak, and M. Stępczak, “Enhanced Mechanical Performance of Resin-Infused 3D-Printed Polymer Lattices,” *Polymers 2025, Vol. 17, Page 1028*, vol. 17, no. 8, p. 1028, Apr. 2025, doi: 10.3390/POLYM17081028.

[27] C. M. S. Vicente, J. Fernandes, L. Reis, A. M. De Deus, M. F. Vaz, and M. Leite, “Effect of protective coatings on the water absorption and mechanical properties of 3D printed PLA,” *Fracture and Structural Integrity*, vol. 13, no. 48, pp. 748–756, Mar. 2019, doi: 10.3221/IGF-ESIS.48.68.

[28] D. Filgueira, S. Holmen, J. K. Melbø, D. Moldes, A. T. Echtermeyer, and G. Chinga-Carrasco, “Enzymatic-Assisted Modification of Thermomechanical Pulp Fibers To Improve the Interfacial Adhesion with Poly(lactic acid) for 3D Printing,” *ACS Sustain Chem Eng*, vol. 5, no. 10, pp. 9338–9346, Oct. 2017, doi: 10.1021/ACSSUSCHEMENG.7B02351.

[29] K. Limpadapun and J. Sukmanee, “A Study of an Effect on Moisture from 3D Printer Filament Drying Processes,” *Key Eng Mater*, vol. 902, pp. 101–106, 2021, doi: 10.4028/WWW.SCIENTIFIC.NET/KEM.902.101.

[30] R. A. Hamid *et al.*, “Effect of Filament Pre-Drying on the Microstructure and Porosity of 3D Printed PLA,” *Journal of Advanced Research in Micro and Nano Engineering*, vol. 24, no. 1, pp. 85–94, Oct. 2024, doi: 10.37934/ARMNE.24.1.8594.

[31] M. Rismalia, S. C. Hidajat, I. G. R. Permana, B. Hadisujoto, M. Muslimin, and F. Triawan, “Infill pattern and density effects on the tensile properties of 3D printed PLA material,” *J Phys Conf Ser*, vol. 1402, no. 4, Dec. 2019, doi: 10.1088/1742-6596/1402/4/044041.

[32] M. Moradi, M. Lalegani Dezaki, E. Kheyri, S. A. Rasouli, M. Aghaee Attar, and M. Bodaghi, “Simultaneous FDM 4D printing and magnetizing of iron-filled polylactic acid polymers,” *J Magn Magn Mater*, vol. 568, p. 170425, Feb. 2023, doi: 10.1016/J.JMMM.2023.170425.

[33] A. D. Banjo, V. Agrawal, M. L. Auad, and A. D. N. Celestine, “Moisture-induced changes in the mechanical behavior of 3D printed polymers,” *Composites Part C: Open Access*, vol. 7, p. 100243, Mar. 2022, doi: 10.1016/J.JCOMC.2022.100243.

[34] R. Heu, S. Shahbazmohamadi, J. Yorston, and P. Capeder, “Target Material Selection for Sputter Coating of SEM Samples,” *Micros Today*, vol. 27, no. 4, pp. 32–36, Jul. 2019, doi: 10.1017/S1551929519000610.

[35] Z. Wang, M. Sun, X. Yao, L. Zhang, and H. Zhang, “Spatiotemporal Variations of Water Vapor Content and Its Relationship with Meteorological Elements in the Third Pole,” *Water 2021, Vol. 13, Page 1856*, vol. 13, no. 13, p. 1856, Jul. 2021, doi: 10.3390/W13131856.

[36] S. Bhagia *et al.*, “Critical review of FDM 3D printing of PLA biocomposites filled with biomass resources, characterization, biodegradability, upcycling and opportunities for

biorefineries," *Appl Mater Today*, vol. 24, p. 101078, Sep. 2021, doi: 10.1016/J.APMT.2021.101078.

[37] B. Li, K. P. Baxevanakis, and V. V. Silberschmidt, "Water Diffusion in Additively Manufactured Polymers: Analysis of the Capillary Effect," *Micro 2024, Vol. 4, Pages 281-294*, vol. 4, no. 2, pp. 281–294, Apr. 2024, doi: 10.3390/MICRO4020017.

[38] F. Comino, P. E. Romero, E. Molero, and M. Ruiz de Adana, "Experimental evaluation of a 3D printed air dehumidification system developed with green desiccant materials," *Appl Therm Eng*, vol. 227, p. 120393, Jun. 2023, doi: 10.1016/J.APPLTHERMALENG.2023.120393.

[39] K. B. Adhikary, S. Pang, and M. P. Staiger, "Long-term moisture absorption and thickness swelling behaviour of recycled thermoplastics reinforced with Pinus radiata sawdust," *Chemical Engineering Journal*, vol. 142, no. 2, pp. 190–198, Aug. 2008, doi: 10.1016/J.CEJ.2007.11.024.

[40] A. Guo *et al.*, "Water absorption rates and mechanical properties of material extrusion-printed continuous carbon fiber-reinforced nylon composites," *Journal of Materials Research and Technology*, vol. 21, pp. 3098–3112, Nov. 2022, doi: 10.1016/J.JMRT.2022.10.134.

[41] D. C. Montgomery and G. C. Runger, *Applied Statistics and Probability for Engineers*, 7th ed., vol. 7. WIley, 2018. Accessed: Dec. 09, 2025. [Online]. Available: https://dl.icdst.org/pdfs/files4/57ca3651c10165f7b64ff0dadf4d4f10.pdf

[42] Gunadi *et al.*, "Comparison of Brake Cooling System on Bus: Simulation and Evaluation of Natural vs Forced Air through Machine Learning Processing," *Journal of Advanced Research in Fluid Mechanics and Thermal Sciences*, vol. 126, no. 2, pp. 178–200, Jan. 2025, doi: 10.37934/ARFMTS.126.2.178200.

[43] R. Hathaway, "Transducers and Data Acquisition," *Fatigue Testing and Analysis: Theory and Practice*, pp. 1–56, Jul. 2004, doi: 10.1016/B978-075067719-6/50002-6.

[44] S. R. Madeti and S. N. Singh, "Monitoring system for photovoltaic plants: A review," *Renewable and Sustainable Energy Reviews*, vol. 67, pp. 1180–1207, Jan. 2017, doi: 10.1016/J.RSER.2016.09.088.

[45] R. A. Hamid, F. H. Hamezah, and J. Abd Razak, "Influence of Humidity on the Tensile Strength of 3D Printed PLA Filament," *Lecture Notes in Mechanical Engineering*, vol. 25, pp. 497–502, 2022, doi: 10.1007/978-981-16-8954-3_47.

[46] C. T. Duarte, N. V. dos Santos, H. F. M. de Queiroz, J. S. S. Neto, D. K. K. Cavalcanti, and M. D. Banea, "Durability Assessment of Additively Manufactured Multi-Material Components for Potential Applications in Structures Exposed to Marine Environments," *J Appl Polym Sci*, vol. 0, p. e70107, 2025, doi: 10.1002/APP.70107;WEBSITE:WEBSITE:PERICLES;WGROUP:STRING:PUBLICATION.

[47] A. Di Schino, Y.-H. Koh, B. Budzí, and K. Federowicz, "Evaluation of PLA and PETG as 3D-Printed Reference Materials for Compressive Strength Testing," *Materials 2025, Vol. 18, Page 3794*, vol. 18, no. 16, p. 3794, Aug. 2025, doi: 10.3390/MA18163794.

[48] A. Aniskevich, O. Bulderberga, and L. Stankevics, "Moisture Sorption and Degradation of Polymer Filaments Used in 3D Printing," *Polymers 2023, Vol. 15, Page 2600*, vol. 15, no. 12, p. 2600, Jun. 2023, doi: 10.3390/POLYM15122600.

[49] J. V. Ecker, A. Haider, I. Burzic, A. Huber, G. Eder, and S. Hild, "Mechanical properties and water absorption behaviour of PLA and PLA/wood composites prepared by 3D

printing and injection moulding," *Rapid Prototyp J*, vol. 25, no. 4, pp. 672–678, Jul. 2019, doi: 10.1108/RPJ-06-2018-0149.

[50] B. Chaudhary, H. Li, and H. Matos, "Long-term mechanical performance of 3D printed thermoplastics in seawater environments," *Results in Materials*, vol. 17, p. 100381, Mar. 2023, doi: 10.1016/J.RINMA.2023.100381.

[51] L. Šimunović, T. Blagec, and S. Meštrović, "Resistance of PETG Materials on Thermocycling and Brushing," *Dent J (Basel)*, vol. 11, no. 5, p. 135, May 2023, doi: 10.3390/DJ11050135/S1.

[52] Ștefan D. Sava *et al.*, "Variations in the Thermomechanical and Structural Properties during the Cooling of Shape-Memory R-PETG," *Polymers (Basel)*, vol. 16, no. 14, p. 1965, Jul. 2024, doi: 10.3390/POLYM16141965/S1.

[53] J. Wu and S. Luo, "Enhancing Printability, Mechanical, and Shape Memory Properties of 4D Printed Linear-Low-Density Polyethylene (LLDPE) Through Blending With Polyethylene Terephthalate Glycol (PETG)," *J Appl Polym Sci*, vol. 142, no. 31, p. e57257, Aug. 2025, doi: 10.1002/APP.57257;REQUESTEDJOURNAL:JOURNAL:10974628;PAGE:STRING:ARTICLE/CHAPTER.

[54] D. D'andrea, G. Risitano, M. Raffaele, F. Cucinotta, and D. Santonocito, "Damage assessment of different FDM-processed materials adopting Infrared Thermography," *Frattura ed Integrita Strutturale*, vol. 16, no. 62, pp. 75–90, Oct. 2022, doi: 10.3221/IGF-ESIS.62.06.

[55] O. Romruen *et al.*, "Impact of environmental storage conditions on properties and stability of a smart bilayer film," *Scientific Reports 2024 14:1*, vol. 14, no. 1, pp. 23038-, Oct. 2024, doi: 10.1038/s41598-024-74004-4.

[56] 3DTrcek, "PLA Drying Temp and Time: Best Practices for Industrial-Grade Results." Accessed: Dec. 10, 2025. [Online]. Available: https://3dtrcek.com/hr/blog/post/pla-drying-temp-and-time-best-practices-for-industrial-grade-results

[57] J. Suder, Z. Bobovsky, M. Safar, J. Mlotek, M. Vocetka, and Z. Zeman, "Experimental analysis of temperature resistance of 3d printed PLA components," *MM Science Journal*, vol. 2021, no. March, pp. 4322–4327, Mar. 2021, doi: 10.17973/MMSJ.2021_03_2021004.

[58] I. Singson, "How to Dry PETG Filament for Perfect Prints." Accessed: Dec. 10, 2025. [Online]. Available: https://siraya.tech/blogs/news/how-to-dry-petg?srsltid=AfmBOopMmtr6OfJ8bk-qTbmqKTtDj-6iPWVia9QPgEpkmR69AMvn944i

[59] M. El Mehtedi, P. Buonadonna, R. El Mohtadi, G. Loi, F. Aymerich, and M. Carta, "Optimizing Milling Parameters for Enhanced Machinability of 3D-Printed Materials: An Analysis of PLA, PETG, and Carbon-Fiber-Reinforced PETG," *Journal of Manufacturing and Materials Processing 2024, Vol. 8, Page 131*, vol. 8, no. 4, p. 131, Jun. 2024, doi: 10.3390/JMMP8040131.

[60] Anycubic, "How to Dry Wet 3D Printer Filament - Simple and Easy Ways | ANYCUBIC 3D Printing." Accessed: Dec. 10, 2025. [Online]. Available: https://store.anycubic.com/blogs/3d-printing-guides/how-to-dry-3d-printer-filament

[61] K. Mirasadi, D. Rahmatabadi, I. Ghasemi, M. Khodaei, M. Baniassadi, and M. Baghani, "Investigating the Effect of ABS on the Mechanical Properties, Morphology, Printability, and 4D Printing of PETG-ABS Blends," *Macromol Mater Eng*, vol. 309,

no. 6, p. 2400038, Jun. 2024, doi: 10.1002/MAME.202400038;PAGE:STRING:ARTICLE/CHAPTER.

[62] J. R. Stojković *et al.*, "An Experimental Study on the Impact of Layer Height and Annealing Parameters on the Tensile Strength and Dimensional Accuracy of FDM 3D Printed Parts," *Materials 2023, Vol. 16, Page 4574*, vol. 16, no. 13, p. 4574, Jun. 2023, doi: 10.3390/MA16134574.

[63] M. A. Dundar, G. S. Dhaliwal, E. Ayorinde, and M. Al-Zubi, "Tensile, compression, and flexural characteristics of acrylonitrile–butadiene–styrene at low strain rates: Experimental and numerical investigation," *Polymers and Polymer Composites*, vol. 29, no. 5, pp. 331–342, Jun. 2021, doi: 10.1177/0967391120916619;WEBSITE:WEBSITE:SAGE;WGROUP:STRING:PUBLICATION.

[64] V. M. Bruère, A. Lion, J. Holtmannspötter, and M. Johlitz, "Under-extrusion challenges for elastic filaments: the influence of moisture on additive manufacturing," *Progress in Additive Manufacturing 2022 7:3*, vol. 7, no. 3, pp. 445–452, Apr. 2022, doi: 10.1007/S40964-022-00300-Y.

[65] N. T. Tuli, S. Khatun, and A. Bin Rashid, "Unlocking the future of precision manufacturing: A comprehensive exploration of 3D printing with fiber-reinforced composites in aerospace, automotive, medical, and consumer industries," *Heliyon*, vol. 10, no. 5, p. e27328, Mar. 2024, doi: 10.1016/J.HELIYON.2024.E27328.

[66] B. Chaudhary, H. Li, and H. Matos, "Long-term mechanical performance of 3D printed thermoplastics in seawater environments," *Results in Materials*, vol. 17, p. 100381, Mar. 2023, doi: 10.1016/J.RINMA.2023.100381.

[67] Y. Zou, W. Zhang, H. Chen, and H. Cheng, "Investigating the Moisture Absorption Behavior of Bamboo Fiber-reinforced Epoxy Composites by Modelling," *Bioresources*, vol. 18, no. 1, pp. 272–290, 2023, doi: 10.15376/BIORES.18.1.272-290.